Petroleum Science 22 (2025) 5277–5295

Contents lists available at ScienceDirect

Petroleum Science

journal homepage: www.keaipublishing.com/en/journals/petroleum-science

Ag-doped ZnO nanoparticles synthesized by *Bacillus subtilis* induce ROS damage and apoptotic activities against sulfate-reducing bacteria cells in oilfields

Yin-Fang Si [a,b,c,d], Yu-Long Liu [e], Fan Zhang [f], Hao Dong [a,c,d], Qing Feng [g], Xiao-Nan Li [g], Yue-Hui She [a,c,d,**], Shan-Shan Sun [a,c,d,*]

[a] *Hubei Key Laboratory of Drilling and Production Engineering for Oil and Gas, Yangtze University, Wuhan, 430100, Hubei, China*
[b] *College of Petroleum Engineering, China University of Petroleum (Beijing), Beijing, 102249, China*
[c] *State Key Laboratory of Low Carbon Catalysis and Carbon Dioxide Utilization, Yangtze University, Wuhan, 430100, Hubei, China*
[d] *School of Petroleum Engineering, Yangtze University, Wuhan, 430100, Hubei, China*
[e] *Oil and Gas Technology Research Institute, Changqing Oilfield Branch, Xi'an, 710018, Shaanxi, China*
[f] *School of Energy Resources, China University of Geosciences (Beijing), Beijing, 100083, China*
[g] *Oilfield Production Optimization Institution of China Oilfield Services Limited, Tianjin, 300459, China*

A R T I C L E I N F O

Article history:
Received 17 June 2024
Received in revised form
29 April 2025
Accepted 21 July 2025
Available online 25 July 2025

Edited by Min Li

Keywords:
B. subtilis
Ag-adopted ZnO nanoparticles
Synthesis mechanism
ROS
Lipid peroxidation injury
Inhibiting sulfate-reducing bacteria

A B S T R A C T

Green-synthesized nanomaterials are anticipated to be extensively applied to inhibit sulfate-reducing bacteria (SRB) in oilfields. Using *Bacillus subtilis* (*B. subtilis*) suspension as the raw material and zinc acetate dihydrate ($C_4H_6O_4Zn \cdot 2H_2O$) along with silver nitrate ($AgNO_3$) as precursors, Ag-ZnO nanoparticles (NPs) were synthesized using a simple and environment-friendly approach. The resulting Ag-ZnO NPs showed a rough surface morphology combined with high dispersibility, showing a particle size distribution of 33–35 nm. Protease and lipopeptides were identified as potential key agents driving the synthesis of Ag-ZnO NPs. At 40 μg/mL, the Ag-ZnO nano-solution effectively inhibited SRB cell growth and reduced the corrosion rate of carbon steel materials induced by SRB. Notably, reactive oxygen species (ROS) and malondialdehyde (MDA) levels increased significantly in SRB cells treated with Ag-ZnO NPs, while cell viability declined, indicating that the nanoparticles caused irreversible damage to SRB biofilms. The inhibitory mechanisms of the NPs against SRB cells were proposed to involve physical electrostatic interactions, metal ion toxicity, cell membrane disruption, and cell lysis.

1. Introduction

Pipeline corrosion, equipment aging, and environmental pollution have always been major problems in the operation of various oilfields (Marciales et al., 2019). One of the main culprits underlying these is the harmful microbial community dominated by sulfate-reducing bacteria (SRB), which exist widely in nature. They produce hydrogen sulfide by reducing sulfate under anaerobic conditions and then participate in the sulfur cycle. Biofilms are complex structure composed of microbial communities and their exopolysaccharides (EPS) (Nwodo et al., 2017). SRB communities adhere to the surfaces of metal materials and form complex biofilm structures, which affect the electrochemical processes on metal surfaces and are the main culprits in microbiologically influenced corrosion (MIC) (Gu et al., 2019). Currently, the main mechanisms of SRB-mediated corrosion include cathodic depolarization (Xu et al., 2016), cell concentration (Okamoto et al., 1983), metabolic product (Jiang et al., 2024), and biologically catalytic cathodic sulfate reduction (BCSR) (Sherar et al., 2011), which have been widely recognized. The formation mechanisms, structural composition, and process of biofilm formation significantly affect the type and rate of metal corrosion reactions. After the SRB colonies reach a certain concentration, they can cause serious

* Corresponding author.
** Corresponding author.
E-mail addresses: sssun33@163.com (S.-S. Sun), sheyuehui@163.com (Y.-H. She).
Peer review under the responsibility of China University of Petroleum (Beijing).

https://doi.org/10.1016/j.petsci.2025.07.015

harm to pipelines and large oilfield equipment (Castaneda and Benetton, 2008). They reduce the service life of such equipment, hinder its operation, and increase the human and material costs associated with on-site maintenance (Khan et al., 2021). Therefore, suppressing and preventing biofilm formation by harmful bacterial communities dominated by SRB are necessary. Based on the aforementioned theories, extensive prevention and inhibition efforts have been carried out against SRB. However, SRB activities can pose a threat to human health under certain circumstances. SRB can lead to corrosion of pipes and equipment, while producing hydrogen sulfide—a toxic gas with a pungent odor that can cause respiratory problems and nervous system damage (Castaneda and Benetton, 2008; Dong et al., 2011). Further, SRB presence in the gut has been linked to the development of some inflammatory bowel diseases, and may affect gut health by producing pro-inflammatory substances. In the environment, sulfides produced by SRB activity react with heavy metals such as arsenic, potentially affecting their bioavailability and toxicity (Utgikar et al., 2002b). Therefore, monitoring and controlling SRB are of great significance to protect human health and environmental safety. Currently, the biocide agents used on a large scale are mostly traditional ones with added toxic reagents (Dugassa and Shukuri, 2017), including oxidizing-type bactericides represented by ozone and chlorine, and non-oxidizing-type bactericides represented by quaternary ammonium salts, phenols, and aldehydes (Rasheed et al., 2019). Although they can inhibit different microbial groups in the oilfield microenvironment, large-scale use causes serious environmental pollution in the long run, which does not conform to the sustainable development of oilfields. Further, traditional antibacterial agents can easily cause bacterial communities to develop resistance (Breijyeh et al., 2020), and long-term use may lead to a decrease in antibacterial efficacy. This necessitates a continuous increase in dosage, leading to the formation of vicious cycle and causing greater harm. Therefore, the synthesis and expanded application of green antibacterial materials are urgently needed (Utgikar et al., 2001a).

Zinc oxide (ZnO) is an inorganic substance. Because of its abundant natural resources, non-toxicity, low-cost, and stable physical and chemical properties, zinc oxide is often considered a cost-effective and excellent antibacterial agent (Iqbal et al., 2022). Compared with traditional chemical disinfection, ZnO NPs present a more stable performance and larger specific surface area (Sun et al., 2019), making them more effective at eliminating microbial populations or single bacteria in water, while significantly reducing time, manpower, and material resource consumption (Stankic et al., 2016). Zinc oxide-based NPs (ZnO NPs) have been widely reported as efficient antibacterial agents suitable for wastewater treatment applications, and have attracted great research interest worldwide (Sirelkhatim et al., 2015). Further, many researchers have prepared functionalized ZnO-based composite nanomaterials through a composite design of morphology and structure, element doping, and other methods to modify and control the morphology and size of ZnO-based nanomaterials, enabling them to exert strong specific functions. For instance, Sayadi et al. (2019) synthesized graphene reinforced with nanocomposites of iron oxide/zinc oxide/tin oxide and evaluated its ability for the photocatalytic degradation of azithromycin in an aqueous environment. Ashar et al. (2019) prepared Fe^{3+}-doped ZnO on polyester fabric using a low temperature hydrothermal method to enhance photocatalytic activity. For ZnO nanomaterials, based on the existing foundation, enhancing the performance of nano-ZnO by doping with Ag is currently a topic of great interest to many researchers. Nano silver is one of the most preferred antimicrobial nanomaterials (Harinee et al., 2022). Ag nanoparticle (NP) coatings have been used to inhibit the growth of bacterial biofilms in medical catheters, prostheses, and heart valves. Ag NP materials have also been widely used to combat the proliferation of various harmful microorganisms, such as *Botrytis cinerea*, *Escherichia coli*, and *Staphylococcus aureus* (Rtimi et al., 2019). Therefore, if excellent Ag and ZnO materials are combined in an appropriate manner, it more nanoscale products with stronger antibacterial properties than those of a single material may be generated. Some researchers have prepared Ag-ZnO NPs by using chemical (Kuriakose et al., 2014), photochemical (Park et al., 2015), precipitation (Subhan et al., 2014), hydrothermal (Alshamsi and Hussein, 2018), microwave (Shao and Wei, 2018), and electrospinning (Pascariu et al., 2020) methods. However, these traditional chemical and physical methods may cause significant harm to the environment, with toxic substances involved in the preparation process.

In recent years, emerging green synthesis methods have received considerable attention from researchers and various industries because of their advantages such as low cost, no use of high-temperature or toxic chemicals, environment-friendliness, ease of operation, and convenience for large-scale production (Tripathy et al., 2010). Green synthesis primarily includes plant synthesis (Satyavani et al., 2011), microbial synthesis (Siddiqi et al., 2018), and algal synthesis (Agarwal et al., 2019). Microbial synthesis has prominent advantages owing to the high growth rate, wide variety, ease of cultivation, and ease of passage with bacteria and fungi (Mahdi et al., 2021). The reported microbial strains used to reduce nano selenium have a relatively low tolerance to zinc acetate and silver nitrate; therefore, screening strains that are more resistant to zinc and silver ions is extremely important for studying the transformation of zinc and silver forms. *Bacillus subtilis* (*B. subtilis*), which is widely distributed in soil and daily life, often forms a wrinkled skin when grown in a liquid culture medium. It is an aerobic bacterium that can produce highly reducing enzymes, lipopeptide surfactants, and other metabolic products (Su et al., 2020). These substances with stability and reducibility are widely involved in green nano synthesis, therefore, *B. subtilis* is considered an excellent raw material for the green synthesis of nanomaterials. Synthesis of Ag-ZnO nanoparticles using *B. subtilis* strains is a suitable choice. *B. subtilis* possesses strong protein expression and secretion abilities, and can produce various reducing enzymes and protein substances, which are necessary for the generation of nanoparticles (Su et al., 2020). Further, it demonstrates excellent physiological characteristics and highly adaptable metabolic functions, enabling it to reproduce rapidly in harsh environments. Moreover, the fermentation cycle of *B. subtilis* is relatively short, approximately 48 h, which can meet the needs of industrial production (Chen et al., 2016). Therefore, *B. subtilis* is considered a high-quality biological nanosynthetic material.

This study aimed to develop a method for the green and efficient synthesis of Ag-ZnO composite nanoparticles using *B. subtilis*. The possible synthesis mechanism was investigated from the microscopic viewpoint. Ag-ZnO composite nanoparticles were found to show significant inhibition effects on oilfield sulfate-reducing bacterial cells, effectively alleviating the pipeline corrosion problem in an oilfield. Overall, this study provides a reference for the practical application of nano-bacteriostatic agents in oilfields and has great application value.

2. Experimental procedures

2.1. Chemicals used

Peptone, sodium chloride, yeast, glucose, sodium sulfate (Na_2SO_4), dipotassium hydrogen phosphate (K_2HPO_4), potassium dihydrogen phosphate (KH_2PO_4), ammonium chloride (NH_4Cl), magnesium sulfate ($MgSO_4$), sodium lactate, zinc acetate ($Zn(CH_3COOH)_2 \cdot 2H_2O$) (99%), silver nitrate ($AgNO_3$), acetone, and glutaraldehyde were obtained from Sinopharm Chemical Reagent Co., Ltd. and were analytically pure. Deionized (DI) water was also used in this study.

2.2. Experimental instruments

A 202-2B electric constant-temperature drying oven (Tianjin Taisite Instrument Manufacturing Factory), H2050R high-capacity high-speed desktop freezing centrifuge (Hunan Xiangyi Laboratory Instrument Development Co., Ltd.), receiving box (Antai Company of Sujing Group), ultraviolet spectrophotometer (Yipu instrument), 202-1AB electric constant-temperature drying oven (Tianjin Taisite Instrument Co., Ltd.), electronic analytical balance (Sartorius Scientific Instrument Co., Ltd.), PHS-2C Precision pH Meter (Hangzhou Qiwei Instrument Co., Ltd.), Malvern Zetasizer NanoZS90 instrument (Malvern Zetasizer, UK); Bruker D8 Advanced X-ray diffractometer (Bruker, Germany), TESCAN MIRALMS scanning electron microscope (TESCAN, Czech Republic), transmission electron microscope (FEI Tecnai AIF20, USA), Agilent NovoCyte Flow cytometer (Agilent Technology' (China) Co., Ltd), Nicolet 6700 Fourier transform infrared spectrometer (Thermo-Scientific, USA), GC-MS (type 7890A-5975C) (Agilent Technologies Co., Ltd.), HSS86.50 Headspace injector (DANI, Italy), and a scientific compass were used in this study.

2.3. Isolation and screening of bacteria

At 37 °C, the target strain for synthesizing bimetallic nanoparticles was isolated from oilfield wastewater. Luria-Bertani (LB) broth is a complex medium known to promote the structural evolution of subpopulations, and contained 5 g of yeast extract, 10 g of trypsin peptone, 10 g of NaCl, and 1000 mL of DI water (Nasiri et al., 2017). LB agar medium, the preferred bacterial growth medium for almost all microbes, including bacteria, fungi, and parasites, was used in this experiment (Sezonov et al., 2007). By adding a high concentration of metal salt solution to the culture medium and measuring the growth status after a period of cultivation, we could determine whether the strain could adapt to a high metallic ion environment and thus obtain higher quality strains and higher nanoparticle yields (Yusof et al., 2020). As low nanoparticle production poses difficulties to large-scale application in oilfields, improving the tolerance of the strain to metallic ions is crucial. The selected strains were inoculated into LB liquid culture medium containing the corresponding mass concentrations of silver acetate and zinc nitrate and incubate at a constant temperature of 37 °C for 48–60 h. The precipitation of the bottom bacterial cells was observed to screen the target strain with strong resistance to both zinc and silver ions.

2.4. Identification of bacteria

The strain BC23 was inoculated onto LB agar plates and colony morphology was observed. Bacterial morphology was observed using scanning electron microscopy. A small amount of bacterial suspension was collected for centrifugation (10,000 rpm, 5 min), washed 2–3 times with DI water to prevent the influence of the culture medium, and used for further identification of 16S rDNA site strains. A bacterial genomic DNA extraction kit was used to extract the total genomic DNA of bacteria. DNA fragments were PCR amplified using universal primers 27F (5-AGAGTT TTGATCCTGGCTCAG-3) and 1492R (5-GGTTACCTTGTTACGACTT-3) for the 16S DNA gene of bacteria. PCR conditions were as follows: pre denaturation at 95 °C for 3 min; 30 cycles of denaturation at 95 °C for 30 s, annealing at 55 °C for 30 s, and extension at 72 °C for 1 min; and final extension at 72 °C for 5 min. The obtained PCR products were sequenced, their homology with known sequences in the NCBI database was compared, and a phylogenetic tree was constructed using MEGA 10.1. The identification process is shown in Fig. 1.

2.5. Green synthesis of Ag-ZnO NPs using *B. subtilis* BC23

The cultivated target strain mentioned earlier was used for the nanosynthesis experiment. Briefly, 5 mL of bacterial suspension was inoculated into 95 mL of LB liquid culture medium and incubated at 37 °C for 48 h. The final OD_{600} was approximately 0.80. A mixed solution of $AgNO_3$ (approximately 40 mg/L) and Zn (CH_3COOH)$\cdot 2H_2O$ (approximately 200 mg/L) was prepared. The mixed solution was added dropwise to the bacterial solution, and stirred continuously until precipitates appeared at the bottom of the conical flask. Then, the mixed solution was placed in a 37 °C constant-temperature shaker for 72 h to obtain a high-purity Ag-ZnO NP crude solution (Datta et al., 2017). In the ultra-clean platform, a negative pressure filtration device was used to obtain the purified product. The pore size of the filter membrane used was 0.22 μm. This operation was used to filter out the interference of bacterial cells as much as possible. The obtained nanoliquid was frozen overnight at −80 °C and the final drying process was completed using a vacuum freeze-drying machine. The final product was obtained as a white powder sample. A centrifuge tube was used for packaging, sealed with a sealing film, and stored (the synthesis process is shown in Fig. 2). The obtained powder was used for further characterization and subsequent antibacterial research.

3. Characterization techniques

The Ag-ZnO NPs were characterized as follows.

a) SEM and EDS were used to observe the morphological characteristics and element distribution. The acceleration voltage was 3 kV when the morphology was analyzed and 25 kV when energy spectrum mapping was performed. The SE2 secondary electron detector was used with a scanning speed of 1°/min.
b) Fourier Transform IR-spectroscopy was performed to analyze the functional groups and bandgap types (ThermoScientific Nicolet6700), with a scanning range of 4000–400 cm^{-1}. Briefly, 1–2 mg of the powder sample and 200 mg of pure KBr were mixed, ground evenly, placed in a mold, and pressed into transparent sheets on an oil press. The sample was then placed into an infrared spectrometer for testing.
c) Wide-angle X-ray diffraction (XRD) was performed to ensure the crystal type using BrukerD8Advance (ZEISSGemini300). A diffractometer with Cu-Kα radiation of $\lambda = 1.54056$ Å, a tube voltage of 40 kV, current of 40 mA, step scanning rate of 0.02°/step, scanning speed of 1°/min, and testing range of 5°–90° (based on the testing requirements) was used.
d) X-ray photoelectron spectroscopy (XPS) was used to determine the elemental composition, chemical state, and molecular structure on the sample surface from the peak position and shape in the XPS map. The source gun type was Al Kα, the analyzer mode was CAE, with a pass energy of 150.0 eV, an energy step size of 1.000 eV, and a total of 1361 energy steps.

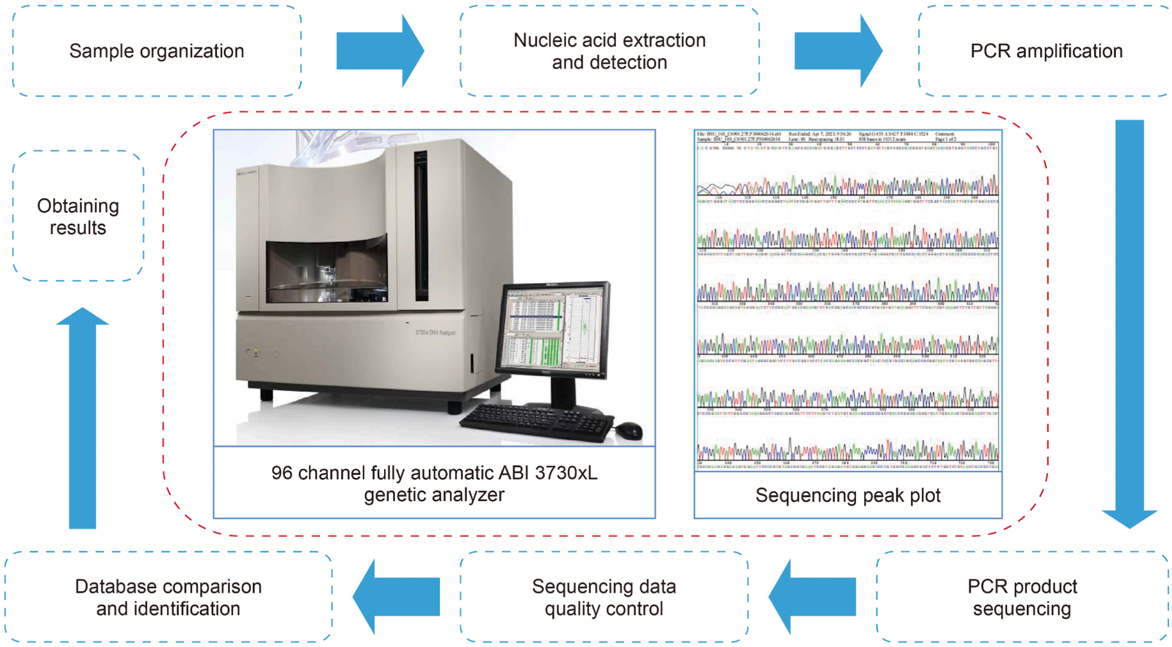

Fig. 1. Flowchart of strain identification.

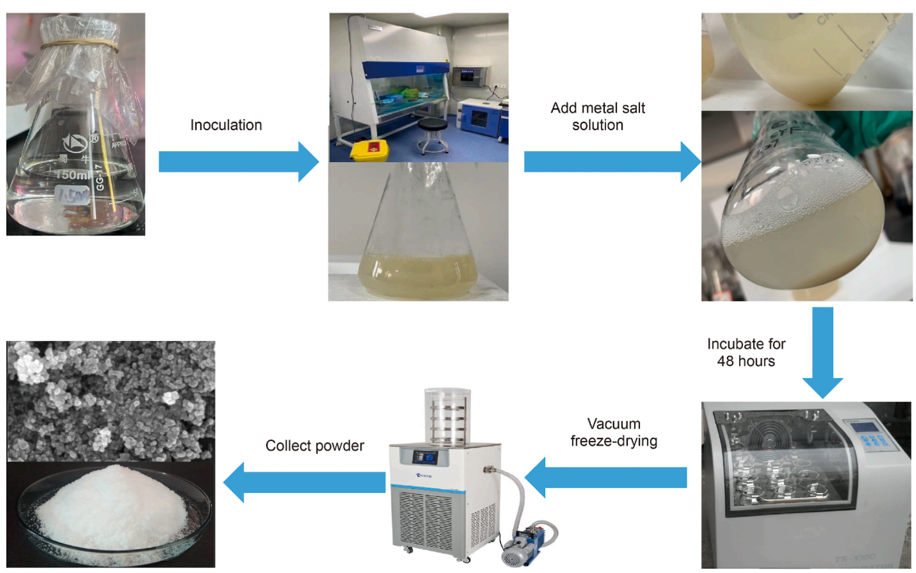

Fig. 2. Synthesis process of Ag-ZnO NPs.

e) Transmission electron microscopy (TEM) (Hitachi-7800) was used to observe the distribution of Ag-ZnO NPs inside and outside the cells. The sample was fixed with 2.5% glutaraldehyde, washed thrice with phosphate buffered saline (PBS), and then subjected to gradient dehydration with acetone. The treated samples were sliced and stained, and the morphologies of the samples were determined using TEM. The acceleration voltage was 200 kV, and the thermal emission electron gun was a W filament.
f) Gas chromatography-mass spectrometry (GC-MS) was used to analyze the active components of the *B. subtilis* BC23 solution. The GC-MS system 7890A-5975C (Agilent Technology Co., Ltd.) was used with the HSS86.50 Headspace injector (DANI, Italy).

3.1. *Metabolite analysis of B. subtilis BC23*

3.1.1. *Enzymatic assay*

1) α-amylase activity

α-amylase catalyzes the endohydrolysis of α-1,4 glycosidic linkages in starch, producing glucose, maltose, etc. Iodine reacts with unhydrolyzed starch to form a starch-iodine complex, which exhibits a characteristic absorption peak at approximately 570 nm. The activity of amylase can be determined by measuring the decrease in absorbance at this wavelength. One unit (U) of α-amylase activity is defined as the amount of enzyme present in 100 mL of supernatant that can hydrolyze 100 mg of starch at 37 °C in 30 min (U/100 mL).

2) Protease activity

The Folin method was used to determine the protease activity of the supernatant of the strain. Under certain temperature and pH conditions, protease generates amino acids containing phenolic groups (such as tyrosine and tryptophan) through hydrolysis. Under alkaline conditions, the content of Folin reagent is reduced to produce molybdenum blue and tungsten blue. Its optical density (OD) at 680 nm was measured by ultraviolet spectrophotometry to calculate its enzyme activity. Protease activity was defined as the amount of enzyme that hydrolyzes casein to produce 1 μg of tyrosine in 1 min. One unit of enzyme activity (U/mL) was expressed as the amount of enzyme producing 1 μg of tyrosine per minute under the assay conditions.

3) Cellulase (CL) activity

The carboxymethyl cellulose sodium (CMC) saccharification force method was used to measure the CL activity in the supernatant of the strain. CL catalyzes the hydrolysis of CMC-Na to produce reducing sugars, which can reduce the nitro group in 3,5-dinitrosalicylic acid to orange amino compounds. The absorbance value was measured at 540 nm wavelength. The absorbance is proportional to the enzyme activity and was used to determine the CL activity. The CL activity unit is defined as 1 mL of enzyme solution hydrolyzing CMC Na to produce 1.0 μ of glucose, which is one enzyme activity unit, expressed in U/mL.

The abovementioned enzyme activity determination tests were conducted using the respective test kits to determine the enzyme activity. Each experiment was repeated three times, with three parallel groups each time.

3.1.2. GC-MS assay

GC-MS (type 7890A-5975C) and the HSS86.50 Headspace injector were used to determine the composition of bacterial metabolites and qualitatively analyze them. The sample was added into the top empty bottle, and the heating temperature was set at 120 °C, the heating time was 20 min, the temperature of the injection valve was 150 °C, the temperature of the transmission line was 180 °C, and the injection volume was 1 mL. The column used was HP-5MS (30.0 m × 250 μm, 0.25 μm). The scanning quality range of mass spectrometry is m/z 29–500. For qualitative analysis, the MS database NIST11 and retention time were used to identify the detected components. The column loss peak was excluded from the database screening results. For quantitative analysis, the area normalization method was used as the quantitative result of the percentage of the peak area for the identified components in the sum of the areas for all identified components. The formula is as follows:

$$C_i = \frac{A_i}{A_1 + A_2 + \ldots + A_i + \ldots + A_n} \times 100\% \tag{1}$$

where C_i is the content of a certain ingredient, %; A_i is the peak area; and n is the total number of the ingredients.

3.2. Antibacterial experiment

SRB mixed strains isolated from oilfield sludge were as indicator bacteria for the antibacterial experiment. Special culture medium was used for SRB, which contained 5.2 g of postgate medium, 1.1 g of D-sodium lactate, and 1000 mL of DI water. First, 200 mL of SRB-specific culture medium was prepared in the experiment, and the pH of the medium was adjusted to approximately 7.5. Before inoculation, high-purity nitrogen gas was blown through the culture medium to maintain anaerobic conditions. The medium was then divided into multiple anaerobic bottles with a capacity of 30 mL for high-temperature sterilization, and the program was set to 110 °C for 15 min. After sterilization, the medium was inoculated with the inoculum to 5%, then cultures at 35 °C for 72 h. A high concentration of black and volatile suspended solids produced in the bacterial solution of an anaerobic flask, indicated sulfate reduction and sulfide production (Enning et al., 2012).

3.2.1. Determination of the MIC of Ag-ZnO NPs

The liquid produced from the oilfield was taken to the laboratory for analysis. Postgate SC medium was prepared and distributed into several 30 mL anaerobic tubes. High concentration nitrogen was injected for deoxygenation to generate an anaerobic environment, and after sterilization at 121 °C for 20 min, it was inoculated with the on-site water sample at 5% in a super-clean workbench. The culture was incubated at 37 °C for more than a week, and passaged every 7 days until the fourth generation. After passage enrichment, the concentration of SRB in the anaerobic bottle was approximately 10^6/mL. Lead acetate test paper was used to further verify whether hydrogen sulfide gas was produced. Determination principle: When the wet lead acetate test paper encounters hydrogen sulfide gas, lead sulfide is produced. If the white test paper immediately turns black, the strain is confirmed to produce hydrogen sulfide gas and a large number of sulfate-reducing bacteria are considered to be present in the sample.

The minimum inhibitory concentration (MIC) is an important indicator for measuring the antibacterial activity of antibacterial drugs (Parvekar et al., 2020). The effect of Ag NPs on SRB activity was determined using a bacteriostatic experiment. Briefly, 9 anaerobic bottles were prepared, 25 mL SRB-specific medium was added to each bottle, and standard SRB culture was inoculated at 5%. The concentration of Ag-ZnO NPs in the medium was 2.5, 5, 10, 20, 40, 80, and 160 μg/mL with the addition of Ag-ZnO NPs in 1–7 bottles according to the double dilution method, and the 8th and 9th bottles left as positive and negative controls. The SRB were incubated in a constant temperature incubator at 37 °C to observe their growth. After culture for a suitable time, 1 mL of bacterial solution was taken, centrifuged, the supernatant was discarded, the suspension was diluted 10 times with deionized water, and absorbance at 600 nm was measured using the U-T6 ultraviolet spectrophotometer. The minimum inhibitory concentration (MIC) was determined by turbidimetry and absorbance data to evaluate the bacteriostatic effect of Ag-ZnO NPs at different concentrations on SRB.

3.2.2. Corrosion rate test

Two groups of steel sheets were selected for the corrosion rate test: one group was untreated carbon steel, and the other was carbon steel treated with Ag-ZnO NPs. For the test, a 0.2 cm × 1 cm × 1 cm carbon steel sheet was used. and the sheet was cleaned to remove impurities, then dried and weighed to record the initial weight. Next, the experimental environment was prepared with a suitable container and solution, and deoxygenated if necessary. The sheet was suspended in the solution, the experimental conditions were set, and the sheet was monitored. After the experiment, the sheet was removed, observed, cleaned in case of corrosion products, dried, and weighed again. The corrosion rate was calculated using the initial and final weights and the results were analyzed. The static weight loss corrosion rate was calculated by measuring the initial mass (W_0), determining the surface area (A), and measuring the final mass (W_1) after the experiment, followed by applying the formula:

$$V = \frac{87600 \times (W_0 - W_1)}{\rho \times A \times t} \tag{2}$$

where V is the corrosion rate, usually measured in miles per year; W_0 is the initial weight before the test, g; W_1 is the weight after the experiment, g; ρ is the density of metal materials, g/m^3; A is the surface area, m^2; t is the experimental time, h.

3.2.3. Cell viability and oxidative damage assessment

The cytotoxicity of Ag-ZnO NPs was evaluated using an MTT assay according to standard protocols. Briefly, cells were seeded in 96-well plates at a density of 5×10^3 cells/well and incubated for 24 h to allow attachment. After treatment with varying concentrations of NPs (0–100 μg/mL) for 24 h, 20 μL of MTT solution (5 mg/mL in PBS) was added to each well, followed by incubation at 37 °C for 4 h in the dark. Subsequently, the culture medium was carefully removed, and 150 μL of dimethyl sulfoxide (DMSO) was added to dissolve the formed formazan crystals. Absorbance was measured at 570 nm using a microplate reader, with a reference wavelength of 630 nm to eliminate the background interference. Untreated cells (culture medium only) and blank controls (medium + MTT + DMSO without cells) were included in parallel. Cell viability (%) was calculated as:

$$\text{Viability}(\%) = \frac{A_{\text{sample}} - A_{\text{blank}}}{A_{\text{control}} - A_{\text{blank}}} \times 100\% \tag{3}$$

where A_{sample}, A_{control}, and A_{blank} represent the absorbance of NP-treated cells, untreated cells, and blank controls, respectively.

The changes in intracellular ROS levels before and after Ag-ZnO NP treatment were measured using the DCFH-DA fluorescent probe. DCFH-DA was diluted in serum-free medium at 1:1000 (from a 10 mM stock) to a final concentration of 10 μM. Cells were harvested and resuspended in diluted DCFH-DA at concentrations ranging from 1 million to 20 million/mL, followed by incubation at 37 °C in the dark for 30 min. After washing twice with cold PBS, the cells were analyzed by flow cytometry. H_2O_2 (200 μM, 1 h treatment) served as the positive control.

ROS is the main initiator of lipid peroxidation reactions (Bedard et al., 2007). In verifying whether Ag-ZnO NPs can cause ROS-related oxidative damage to SRB cells, the malondialdehyde (MDA) content was measured to quantify the degree of lipid peroxidation in the bacteria (Tirani and Haghjou, 2019). Bacterial cells were centrifuged and collected in a centrifuge tube. The sample was treated according to the ratio of the number of bacteria (10^4) and the volume of the extraction solution (mL) as (500–1000):1. The sample was crushed using an ice bath ultrasound (power 20%, ultrasound for 3 s, followed by an interval of 10 s, repeated 30 times), centrifuged for 10 min at 8000 rpm at 4 °C, and the supernatant was obtained for later use. The specified reagent was added to the measuring and reference tubes, boiled in water for 60 min, cooled to room temperature, centrifuged, and the supernatant was obtained for observation using a UV spectrophotometer.

3.3. SRB community analysis

To further validate the inhibitory effect of Ag-ZnO NPs on sulfate reducing bacteria, the biodiversity analysis of SRB treated with Ag-ZnO NPs and the SRB treated with no Ag-ZnO NPs was performed to determine the inhibitory effect of Ag- ZnO NPs on SRB. Cultures treated with Ag-ZnO NPs were collected and cultured for 10 days for characterization, and the control group was prepared. The concentration and purity of DNA were determined by 0.8% agarose gel electrophoresis. Primers 338F (5′-ACTCCTACGGGAGGCAGCA-3′) and 806R (5′-TCGGACTACHVGGGTWTCTAAT-3′) targeting the V3–V4 region of the bacterial 16S rDNA gene were used for PCR amplification. The PCR products were sequenced using the Illumina MiSeq platform for high-throughput sequencing. The DADA2 method of QIIME2 software was used to remove primers and denoise the sequence, and the NCBI database comparison results were used to annotate the sequence for taxonomic analysis (Porter and Hajibabaei, 2018). By performing percentage statistics on the number of sequences (absolute abundance values) and species, the relative abundance of different species genes at each taxonomic level was obtained.

4. Results and discussion

4.1. Isolation and screening of bacteria

In all, 13 bacterial strains with different morphologies were isolated and purified, 6 strains with better growth were selected and named BC20, BC21, BC22, BC23, BC24, and BC25 for liquid culture experiments. The results of re-screening are shown in Table 1. Strain BC23 with strong resistance to silver and zinc ions was screened and compared, showing the highest tolerance to $AgNO_3$ and zinc acetate reaching 40 and 200 mg/L. Chen et al. (2015) isolated the salt-tolerant strain A375 with a tolerance concentration of 0.010 mmol/L to $AgNO_3$, while salt-tolerant strain A381 showed a tolerance concentration of 0.2 mmol/L to $ZnSO_4$. Compared with the reported double salt resistant Ag-Zn strains, BC23 showed a higher tolerance to $AgNO_3$ and zinc acetate, which is beneficial for the biological preparation of Ag-ZnO NPs.

4.2. Bacterial identification

As shown in Fig. 3(a), the colonies of Strain BC23 are generally white with obvious wrinkles on the surface. The morphology of bacterial cells under bioelectron microscopy is shown in Fig. 3(b); the bacteria are short, rod-shaped with slight shrinkage and uniform distribution.

The DNA-barcoding sequence refers to the standard, sufficiently variable, easily amplified, and relatively short DNA fragment that can represent the species in the organism. Currently, the DNA-barcoding fragments for microbial identification mainly include 16S rDNA (bacteria), 26S rDNA (yeast), or ITS (fungi) fragments (Estensmo et al., 2021). DNA-barcoding fragments corresponding to the strain were amplified by PCR, their DNA sequences were obtained using the gold standard sequencing method (Sanger sequencing), followed by comparative analysis in the NCBI database (Haas et al., 2011). In general, if the sequence similarity reached >97%, it could be considered the same strain. The DNA of strain BC23 was extracted, and its 16S rDNA was amplified using 27F and 1492R as primers. The product was a

Table 1
Precipitation of different bacterial strains under double salt Ag-Zn concentrations.

Strain number	Mass concentration of silver nitrate, mg/L					
	10	20	30	40	50	60
	Mass concentration of zinc acetate, mg/L					
	50	100	150	200	250	300
BC20	+++	++	+	–	-	-
BC21	+++	+++	++	+	-	-
BC22	+++	++	+	+	-	-
BC23	++++	+++	+++	+++	++	+
BC24	+++	+	+	-	-	-
BC25	+++	++	+	-	-	-

Note: ++++ more, +++ normal, ++ small, + trace, - clear.

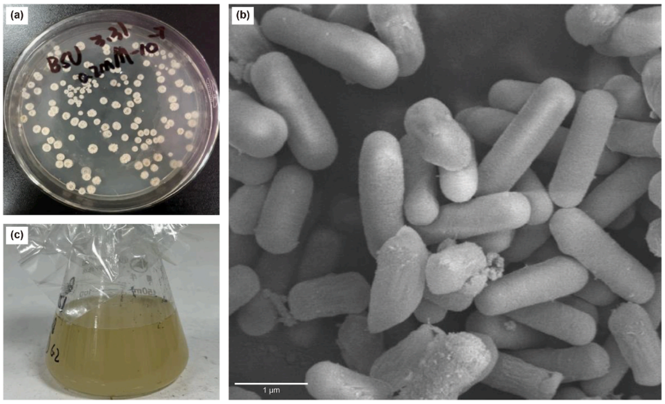

Fig. 3. Morphological characteristics of *B. subtilis.* **(a)** *B. subtilis* colony, **(b)** bioelectron microscopic image of *B. subtilis*, **(c)** *B. subtilis* suspension.

fragment of approximately 1500 bp in 1 g/dL agarose gel electrophoresis, clear and without heterobands. Well-sequenced splicing sequences were compared in the rRNA/ITS databases of NCBI and sorted in accordance with the scores; the best match was provided as the identification result, multiple sequence alignment was performed and the genetic evolution tree was constructed in MEGA 7.0 software. Strain BC23 and the *B. subtilis* were found to be parallel within the local node range, with a 100% similarity in their nucleotide sequences. The phylogenetic tree (constructed by N-J method) is shown in Fig. 4. The red mark in the figure indicates the strain isolated in this study, which has been identified as *B. subtilis* BC23.

4.3. SEM/EDS

The size and morphological characteristics of Ag-ZnO NPs were determined using high-resolution scanning electron microscopy (Fig. 5). Semiquantitative scanning was performed using an external X-ray energy chromatograph to understand the elemental distribution and relative content of the material. a spherical NP with a particle size of approximately 35 nm was clearly observed in the sample, with a uniform distribution and size.

Energy dispersive X-ray spectrometry (EDS) is an analytical technique that allows for the chemical characterization/elemental analysis of materials (Scimeca et al., 2018). An EDS detector was added to the electron microscope. When the electron probe scans the sample, characteristic X-rays are emitted and measured, and each recorded EDS spectrum corresponds to a specific position on the sample. Elements can be identified based on the position of the peaks in the spectrum, and the intensity of the signal corresponds to the concentration of the elements (Newbury and Ritchie, 2013). The quality of the results generally depends on the signal intensity

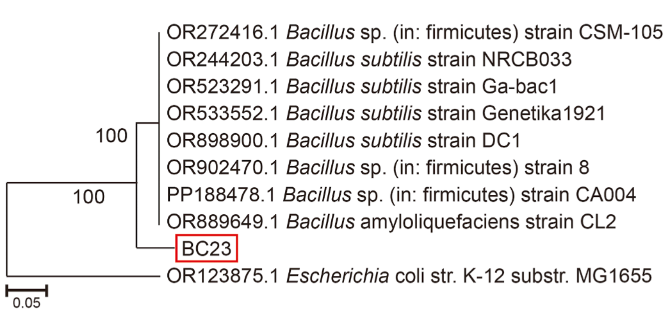

Fig. 4. Phylogenetic tree of strain BC23.

and spectral purity. The signal strength largely depends on a good signal-to-noise ratio, especially for trace element detection and dose minimization. Further, purity affects the number of visible false peaks (Cliff and Lorimer, 1975). The EDS surface scanning results and elemental semi-quantitative results are shown in Fig. 6. To some extent, the EDS results represent the types and corresponding proportions of elements within a certain local range. First, the results showed the presence of a certain amount of C, N, O, S, Cl, Zn, Ag elements in the sample. Two important concepts of excitation voltage and acceleration voltage need to be considered here. In general, the acceleration voltage is chosen to be 2–3 times the excitation voltage of the element. The minimum excitation voltage for Ag, Zn, and O is 22.166, 8.637, and 0.523, respectively. Because of the significant difference in excitation voltage among these three core elements, choosing the correct acceleration voltage, which closely affects the number of excited electrons and the detected graph results, is crucial (Edwards et al., 2014). Therefore, in this experiment, a comprehensive consideration is given to selecting 25 keV. However, regardless of the choice, some tolerable errors are unavoidable.

The mass percentage ratio of Ag to Zn is approximately 1:4, which may be related to the molar concentration of elements in the precursor solution and uneven doping of the two types of nanoparticles, consistent with the EDX results of (Thabit et al., 2022). Further the presence of C, N, and S elements may be attributed to the presence of certain organic compounds in the sample, such as bacterial metabolites (such as proteins) and interference from a small amount of residual culture medium. Therefore, the resulting nanosample contains a small number of impurities. However, this does not affect its antibacterial performance, which has been verified in subsequent experiments. The EDS results further indicate that the synthesis of Ag-ZnO NPs using *B. subtilis* is feasible.

4.4. FTIR

The functional group categories of *B. subtilis* bacterial solution Ag-ZnO NPs are shown in Fig. 7. In the biosynthesis of Ag-ZnO NPs by *B. subtilis* strains, proteins are involved in Ag^{+} and Zn^{2+} reduction and the anisotropic growth of Ag-ZnO NPs. The biological functional group interaction between *B. subtilis* and the nanoparticles was analyzed using infrared spectroscopy. The infrared spectrum of the *B. subtilis* bacterial suspension shows characteristic peaks at 3371, 2974, 1582, 1410, 1064, 861, 695, and 543 cm^{-1}. The infrared spectra of Ag-ZnO NPs show characteristic peaks at 3391, 2933, 1592, 1417, 1033, 1074, 771, and 634 cm^{-1}. From the comparison of the two FTIR spectra, the positions of the peaks are basically the same, with differences in the intensity of the detected peaks at the same position. The differences in intensity may be related to the role played by the substance in the nano-synthesis process, or may be related to the excited electrons. This result is consistent with the results of Ghosh et al. (2012). An absorption peak above 3000 cm^{-1} indicates the presence of unsaturated (C–H) stretching vibrations, which may indicate olefins, alkynes, or aromatic compounds; an absorption peak below 3000 cm^{-1} indicates the presence of saturated (C–H) stretching vibration absorption. For nanoliquid samples, the absorption peaks observed at 3391, 1592, and 1033 cm^{-1} correspond to O–H, C–O, and N–H stretching vibrations, indicating the presence of protein-like substances. The peaks at 2933 and 1417 cm^{-1} are attributed to (C–H) stretching vibration and the side chains of (COO–) carboxyl groups (Gopinath and Velusamy, 2013), whereas the peaks at 772 cm^{-1} indicate out of plane bending of O–H, indicating the possible presence of aromatic and aliphatic substances, which may be attributed to the cell membrane (Rasool

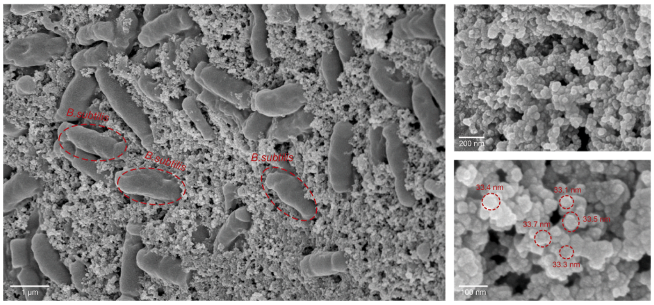

Fig. 5. Scanning electron microscopy of Ag-ZnO NPs.

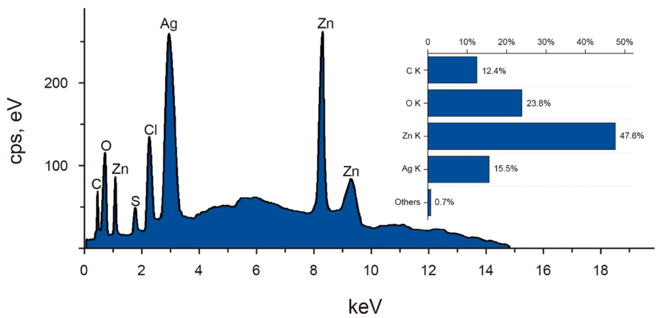

Fig. 6. EDS spectra of Ag-ZnO NPs.

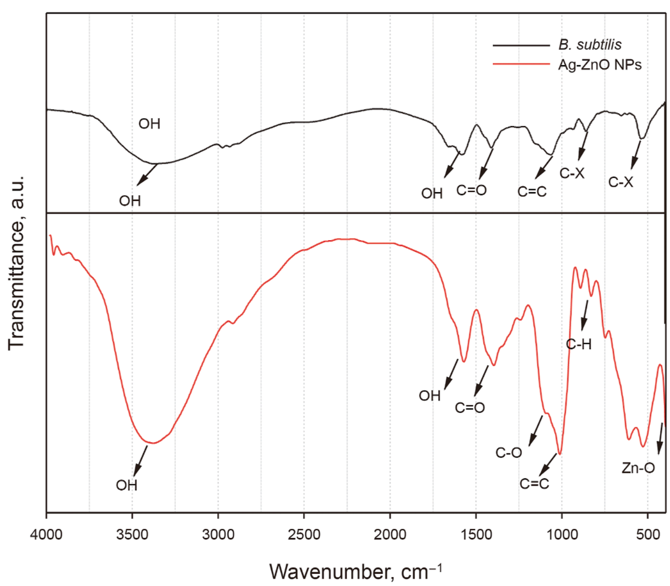

Fig. 7. Fourier transform infrared spectroscopy results of *B. subtilis* and Ag-ZnO NPs.

et al., 2018). Negatively charged groups can interact with NPs through electrostatic interactions. Therefore, the protein molecules metabolized by *B. subtilis* can serve as stabilizers for NPs. Meanwhile, the characteristic peak at 1074 cm^{-1} indicates the presence of stretching vibration bands in the aliphatic amine C–N, while the amine bonds in the protein have strong metal binding ability. Therefore, the good dispersibility of Ag-ZnO NPs may be attributed to the protein coating of metal NPs, which plays a significant role in preventing the aggregation of nanoparticles and promoting their stability in the culture medium. From the observed FTIR spectrum results, we concluded that the protein present in the *B. subtilis* metabolites could be accountable for the production as well as stabilization of Ag-ZnO NPs.

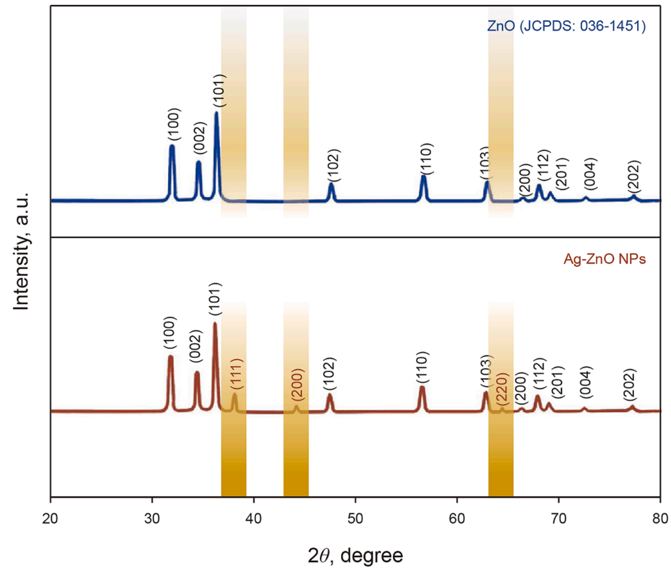

Fig. 8. X-ray diffraction results of Ag-ZnO NPs (Si et al., 2024).

4.5. XRD

The XRD spectra of Ag-ZnO NPs are shown in Fig. 8. Peaks at 31.76°, 34.41°, 36.24°, 47.62°, 56.54°, 62.88°, and 67.82° were observed from the lattice planes (100), (002), (101), (102), (110), (103), and (112), respectively. Characteristic peaks were observed at the values, and they matched well with the pure ZnO structure (JCPDS, No.36-1451), in accordance with the hexagonal structure with good crystallinity (Yousefi et al., 2015). Further, Ag reflects at 38.04°, 44.30°, and 77.35° along the lattice planes (111), (200), and (311) (JCPDS, No.04-0783). The result proves the exact existence of Ag-ZnO NPs crystals. For the synthesized Ag-ZnO composite nanostructures, grain orientation was observed along the *c*-axis (101) plane. A lack of shift in the peak positions of Ag-ZnO nanocomposites indicates that Ag particles are positioned on the surfaces of the crystalline ZnO NPs. Compared with the XRD spectra obtained from the standard card data of pure ZnO, i.e., cubic wurtzite, the peak intensity along the (101) direction remained consistent in both spectra. The uneven nucleation of grains is speculated to be caused by the presence of Ag^{+}, consistent with the viewpoint of Indhira et al. (2022). The significantly larger radius of Ag^{+} (0.126 nm) compared with that of Zn^{2+} (0.070 nm) is a possible reason for the existence of the secondary crystalline phase in the Ag-ZnO samples. The difference between the radius of Ag^{+} and Zn^{2+} limits the solubility of Ag in the Zn lattice site. Considering that the ionic radius of Ag (0.126 Å) was smaller than that of Zn (0.74 Å), Ag doping may be beneficial to reduce the crystal size of the NPs under the same conditions compared with that of pure ZnO NPs, providing a reference research direction for subsequent experiments.

4.6. XPS

XPS examines the valence state of prepared Ag-doped ZnO nanomaterial exhibited in Fig. 9(a)–(e). The binding energies in the XPS spectra presented in Fig. 3 are calibrated using that of C 1s (285.2 eV). In Fig. 9(a), all the peaks on the curve are ascribed to Ag,

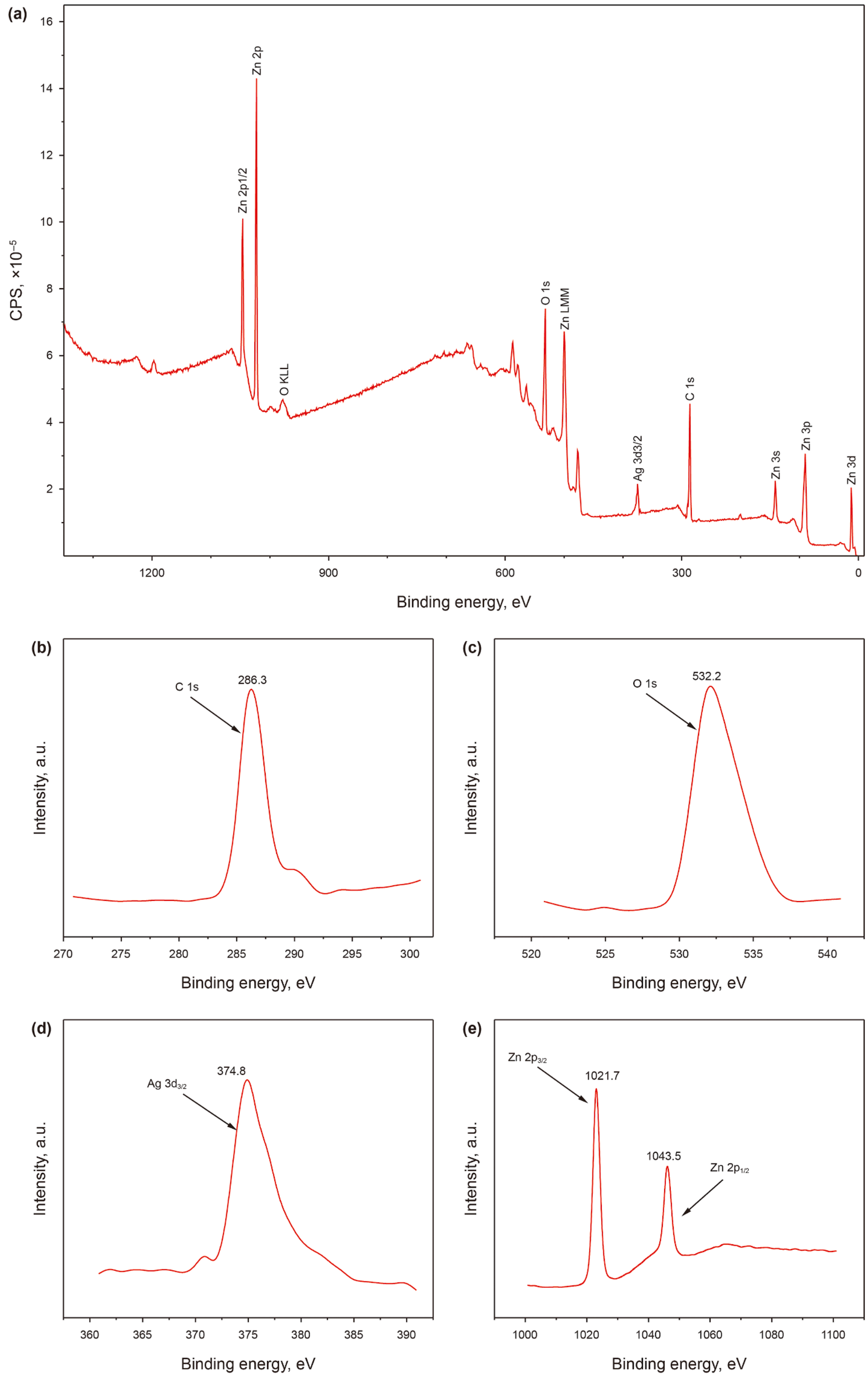

Fig. 9. XPS spectra of the as-synthesized sample. **(a)** Full XPS spectrum of the sample; **(b)** C 1s spectrum; **(c)** O 1s spectrum; **(d)** Ag 3d spectrum; and **(e)** Zn 2p spectrum.

Zn, O, and C elements and no peaks of any other elements are observed. The presence of the C peak is consistent with the EDS elemental analysis results shown in Fig. 9. This can be attributed to the specific organic components derived from microbial metabolites. Furthermore, this observation provides strong support for the subsequent GC-MS results discussed in the following section. Therefore, we concluded that the sample was composed of three elements, Zn, Ag, and O, which was in good agreement with the abovementioned XRD and SEM/EDS results. The peaks at 286.3, 532.2, 374.8, 1021.7, and 1043.5 eV indicate the existence of C 1s, O 1s, Ag 3d, and Zn 2p. The peaks appearing in Fig. 9(d) and (e) are symmetric and center at 367.2, 1021.7, and 1043.5 eV, attributed to Ag $3d_{3/2}$, Zn $2p_{3/2}$, and Zn $2p_{1/2}$, respectively. The results of C, O, Ag, and Zn indicate good formation of the Ag-doped ZnO nanomaterial in the XPS spectrum (Zheng et al., 2007; Potlog et al., 2015).

4.7. Enzymatic assay

The *B. subtilis* used in this experiment is simple to cultivate, easy to reproduce and expand, and can adapt to harsh living

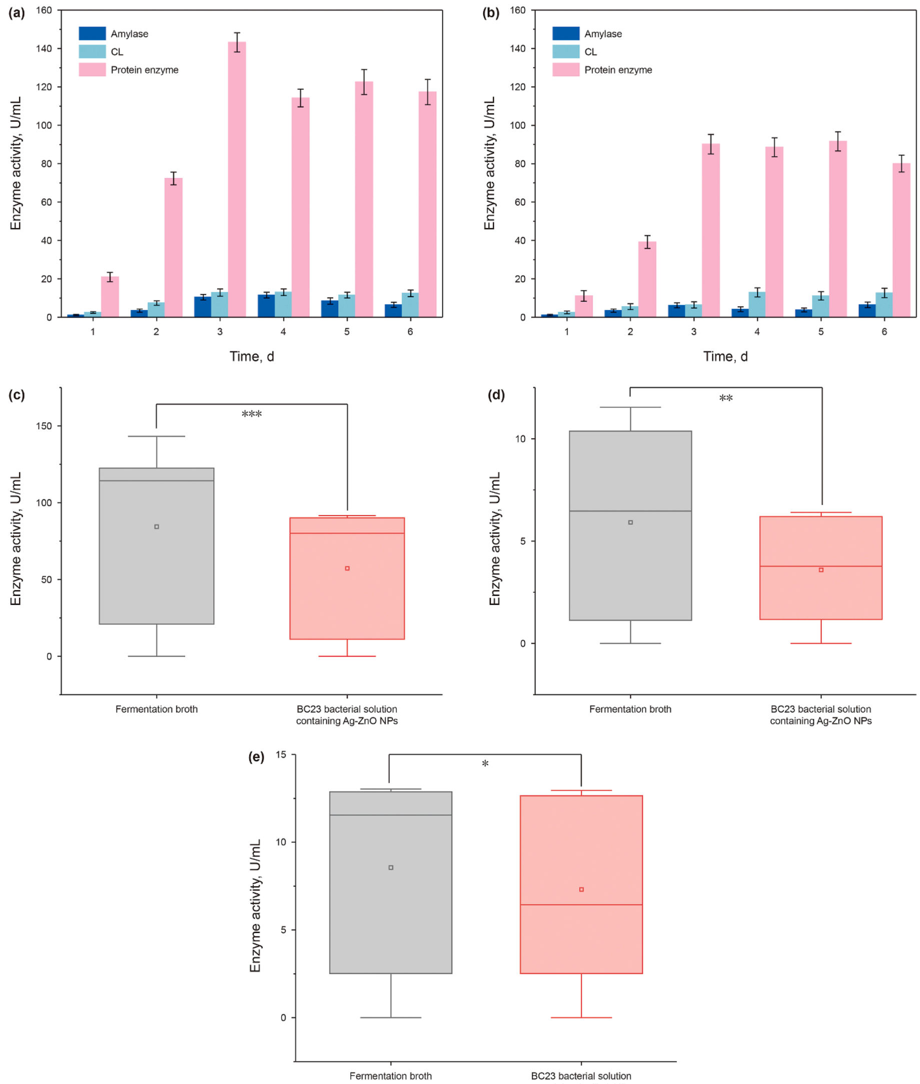

Fig. 10. Enzyme activity in strain BC23. **(a)** Fermentation broth, **(b)** BC23 bacterial solution containing Ag-ZnO NPs, and significance analysis of **(c)** α-amylase, **(d)** protease, **(e)** cellulase (CL) enzyme activity for (a) and (b).

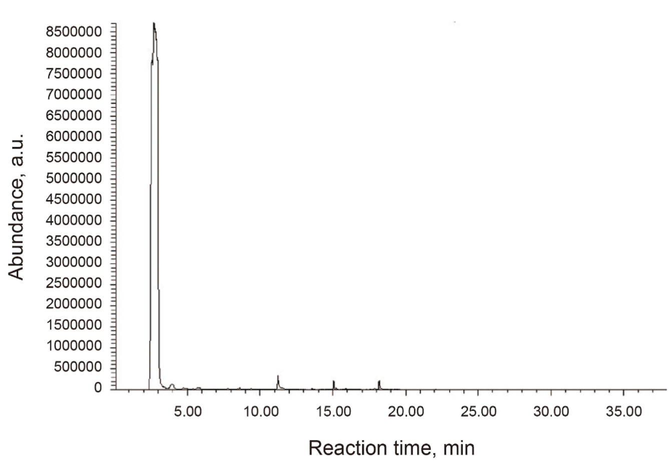

Fig. 11. Total ion map of *B. subtilis* fermentation.

environments, making it an ideal raw material for synthesizing nanomaterials. The self-differentiation function of *B. subtilis* is powerful, and can synthesize α-enzymes such as amylase, protease, and cellulase (CL) (Puhazhselvan et al., 2017), which are used to achieve synergistic nanosynthesis inside and outside the cells. The activity of amylase, protease, and CL is shown Fig. 10. Fig. 10(a) shows the enzyme activity results of strain BC23 after 6 days of cultivation. Strain BC23 could produce three enzymes simultaneously, of which protease activity was the highest, 143.27 U/mL and amylase activity was the lowest, 11.23 U/mL. The CL activity was intermediate, and its activity value was 13.21 U/mL. Fig. 10(b) shows the enzyme activity of the bacterial solution of Strain BC23 during nanomaterial synthesis; the highest activity values of the protease, amylase, and CL were 85.61, 10.73, and 7.63 U/mL, respectively. The protease activity decreased, but still existed at a higher level, possibly because of the loss of protease in metal reduction during the Ag nanoparticle synthesis. However, the activity of amylase and CL is relatively low, which may be attributed

Table 2
Main products of the fermentation metabolism of *B. subtilis*.

Name	Molecular formula	Matching degree	Molecular weight, amu	Qualitative analysis, %
Benzene, 1-methyl-3-(1-methylethyl)-	$C_{10}H_{14}$	83	134.11	2.85
Cyclohexanemethanol,.alpha.,.alpha.,4-trimethyl-	$C_{10}H_2O$	83	156.15	23.97
Tricyclo[5.4.0.0(2,8)]undec-9-ene, 2,6,6,9-tetramethyl-, (1R,2S,7R,8R)-	$C_{15}H_{24}$	96	204.19	0.6
1,2,4-Methenoazulene, decahydro-1,5,5,8a-tetramethyl-, [1S-(1.alpha.,2.alpha.,3a.beta.,4.alpha.,8a.beta.,9R*)]-	$C_{15}H_{24}$	90	204.19	1.14
10s,11s-Himachala-3(12),4-diene	$C_{15}H_{24}$	87	204.19	0.51
Longifolene	$C_{15}H_{24}$	99	204.19	8.44
Caryophyllene	$C_{15}H_{24}$	93	204.19	2.78
1,4,7,-Cycloundecatriene, 1,5,9,9-tetramethyl-, Z,Z,Z-	$C_{15}H_{24}$	70	204.19	0.85
Naphthalene, 1,2,4a,5,8,8a-hexahydro-4,7-dimethyl-1-(1-methylethyl)-, [1S-(1.alpha.,4a.beta.,8a.alpha.)]-	$C_{15}H_{24}$	93	204.19	0.83
(−)-Spathulenol	$C_{15}H_{24}O$	68	220.18	0.73
trans-Geranylgeraniol	$C_{20}H_{34}O$	47	290.26	2.13
1,4-Methanoazulen-9-ol, decahydro-1,5,5,8a-tetramethyl-, [1R-(1.alpha …	$C_{15}H_{26}O$	90	222.2	11.82
.beta.-Humulene	$C_{15}H_{24}$	80	204.19	0.89
cis-Thujopsene	$C_{15}H_{24}$	55	204.19	0.31
Tricyclo[5.4.0.0(2,8)]undec-9-ene, 2,6,6,9-tetramethyl-, (1R,2S,7R,8R)-	$C_{15}H_{24}$	46	204.19	0.02

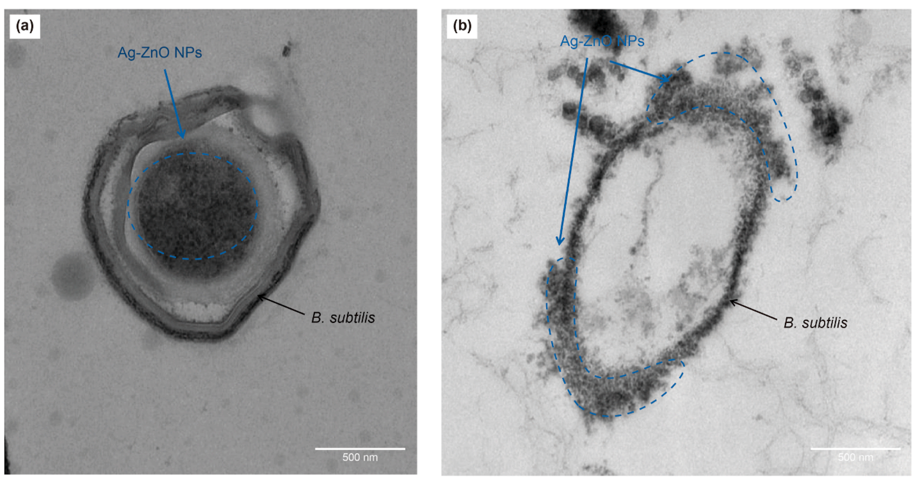

Fig. 12. TEM of Ag-ZnO NPs with *B. subtilis*.

to the addition of metal ions inhibiting the synthesis of some enzymes. Therefore, amylase and CL are the main reasons for nanosynthesis as well as important for the synthesis process. Fig. 10(c), (d), and (e) respectively show the significance analysis results of α-amylase, protease, and CL enzyme activity in the BC23 fermentation broth and the bacterial solution producing Ag-ZnO NPs, which further reveal that the protease is one of the main factors promoting the synthesis of Ag-ZnO NPs. Amylase and protease belong to extracellular enzymes (Puhazhselvan et al., 2017), and exist in an extracellular environment; CL is an intracellular enzyme (Reddy et al., 2022), which exists in the cell and has a low content. *B. subtilis* can produce reducing enzymes both inside and outside the cell, and these three enzymes along with other protein molecules play a crucial role in synthesizing Ag-ZnO NPs.

4.8. GC-MS analysis

The total ion flow diagram of *B. subtilis* BC23 is shown in Fig. 11. The NIST database was used for searching; then, polyoxosilane (column loss component) and other impurity peaks were deducted. After each component in the mixture was identified by peak area normalization and the relative percentage of each component was calculated, 17 compounds with high matching degree were isolated and identified, as shown in Table 2. Among these, the relatively large content of substances mainly included: cyclohexanemethanol,.alpha.,.alpha.,4-trimethyl-, 1,4-Methanoazulen-9-ol, decahydro-1,5,5,8a-tetramethyl-, [1R-(1.alpha.., Longifolene, Benzene, 1-methyl-3-(1-methylethyl)-, caryophyllene, and trans-geranylgeraniol. These substances are mainly lipopeptides and terpenes, and include small amounts of alcohols.

4.9. Analysis of the Ag-ZnO NP synthesis mechanism

Fig. 12 demonstrates nanoparticle synthesis in both intracellular and extracellular regions of *B. subtilis*. Moreover, more nanoparticles were produced outside the cell than inside the cell, possibly because protease plays an important role as an extracellular enzyme. Both are the effective methods of synthesis. Metal ions were adsorbed on the outside of *B. subtilis* cells and slowly entered their inside to achieve nanoparticle synthesis through biological action. This is consistent with the findings of Feng et al. (2021). For bacteria and fungi, enzymes and proteins in microbial cells are the main entities involved in intracellular or extracellular redox. Regarding intracellular synthesis, the enzymes (such as lactate dehydrogenase) and proteins inside the cell are abundant. When metal ions enter the cell, these reducing substances synergistically reduce metal ions into metal NPs. Extracellular synthesis is related to microbial cell metabolism. Its abundant metabolic substances are discharged outside the cell, causing the external

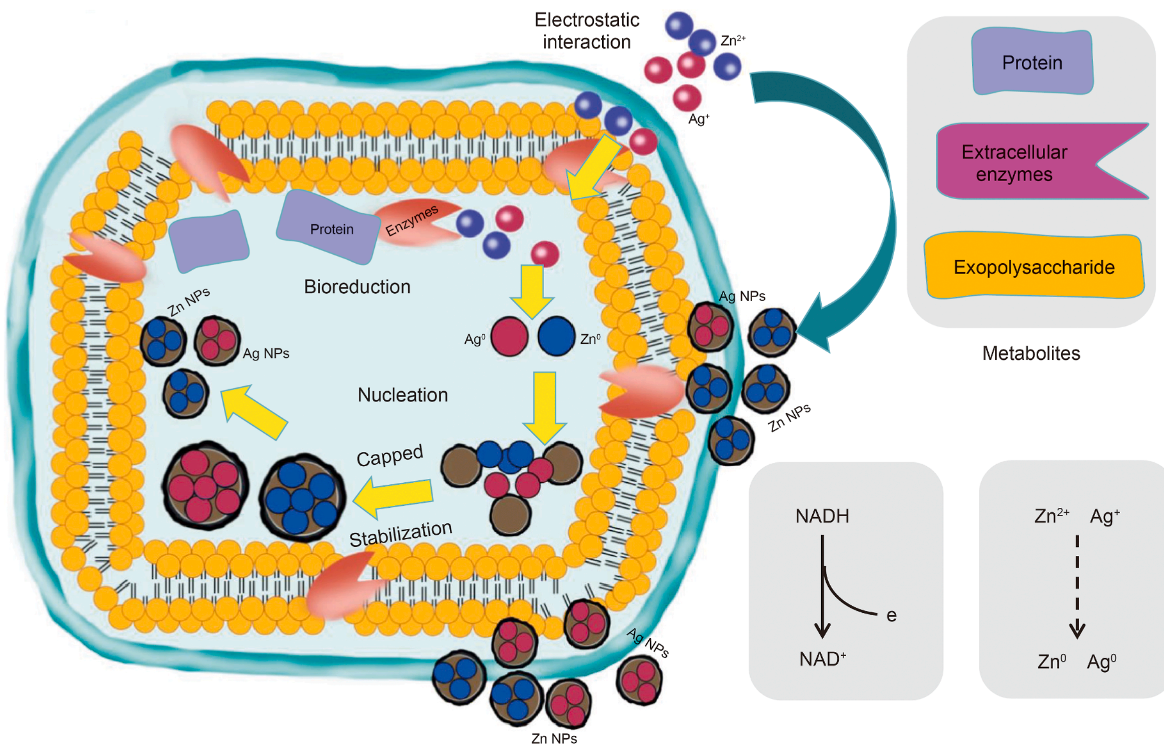

Fig. 13. Biosynthesis mechanism of Ag-ZnO NPs.

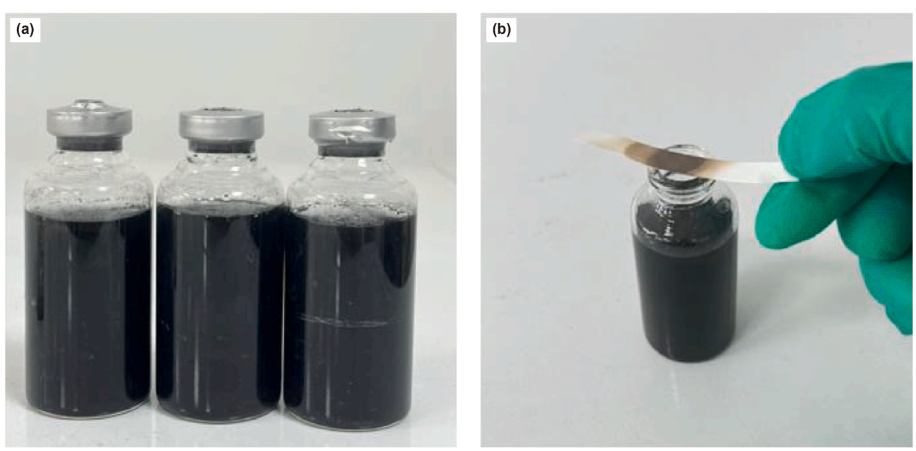

Fig. 14. **(A)** SRB after passage culture, **(b)** reaction with lead acetate test paper.

environment of the cell to be filled with reducing substances, which promote the reduction of metal ions. Many reports have shown that some fungi, such as *Cladosporium*, *B. licheniformis*, *Fusarium oxysporum*, and *Penicillium brevis*, can use nitrate reductase to synthesize metal NPs (Ovais et al., 2018). The schematic diagram of the synthesis mechanism obtained through comprehensive consideration is shown in Fig. 13.

4.10. MIC determination

After a 48-h culture with the on-site water sample, thick black substances (FeS) appeared on the inner wall of the bottle. After taking one sample and opening the lid, a pungent H_2S smell was detected, as shown in Fig. 14. The lead acetate test paper placed at the mouth of the bottle changed color, indicating that the produced liquid of the oilfield contained SRB. With increasing culture time, the black sediment in the medium increased significantly, indicating active SRB growth in the sample. The SRB were growing well.

The inhibitory effect of Ag-ZnO nanocomposites on SRB growth is shown in Figs. 15 and 16. Sample A was the positive control group and I was the negative control group. The mass concentrations of Ag-ZnO NPs in B, C, D, E, F, G, and H were 2.5, 5, 10, 20, 40, 80, and 160 μg/mL, respectively. The addition of Ag-ZnO NPs significantly delayed the logarithmic growth of SRB and reduced the number of bacteria. When the concentration of Ag-ZnO NPs reached 20 μg/mL, the number of sulfate-reducing bacteria remained at a low level compared with that in the control group,

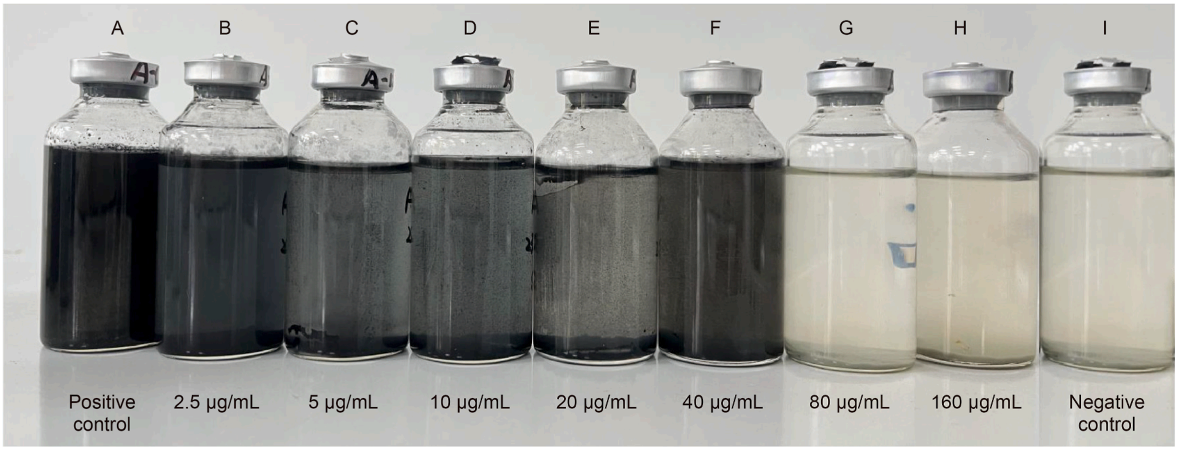

Fig. 15. Inhibitory effect of Ag-ZnO NPs on the growth of SRB.

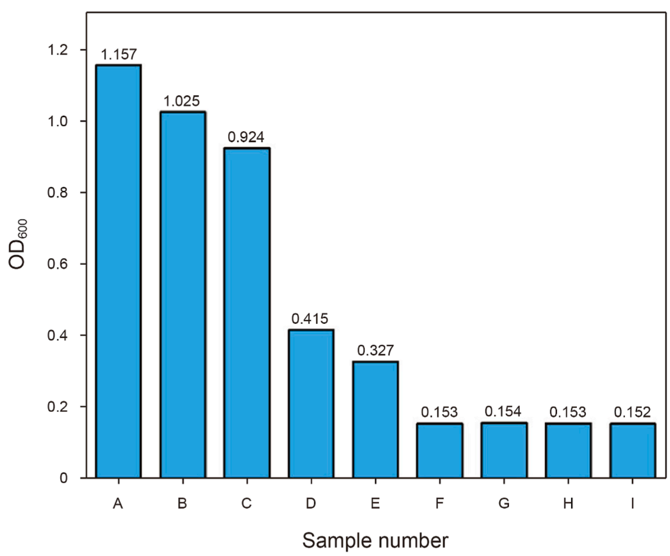

Fig. 16. Absorption values of SRB samples treated with different concentrations of Ag-ZnO NPs.

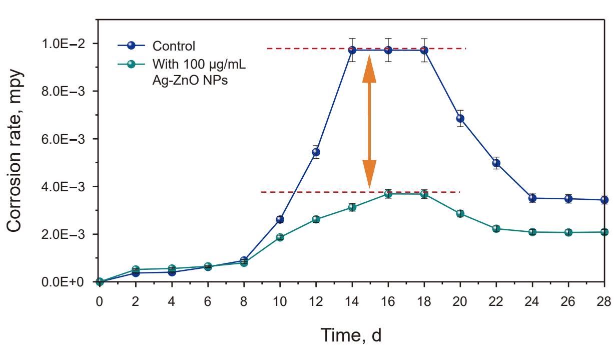

Fig. 17. The relationship between the corrosion rate of the steel sheet and time.

and the absorbance measured at 600 nm was approximately 0.327, indicating that 20 μg/mL Ag-ZnO NPs had a good inhibitory effect on SRB. When the concentration of Ag-ZnO NPs in SRB-containing medium reached 40 μg/mL, their inhibitory effect on SRB began to be similar, and the bacterial fluid was clear and transparent without black sulfide production, highly similar to the negative control group. The very low absorbance of the sample at 600 nm further indicates that Ag-ZnO NPs has an excellent inhibitory effect on SRB at this concentration, and that the minimum inhibitory concentration of Ag-ZnO NPs on SRB is 40 μg/mL.

4.11. Corrosion rate test

Fig. 17 compares the corrosion rates over one month between the blank group and the Ag-ZnO nanoparticle-coated carbon steel in SRB (sulfate-reducing bacteria)-containing medium. The blank group comprised untreated carbon steel plates, whereas the other group included Ag-ZnO nanoparticle-coated carbon steel plates. Notably, the corrosion rate of the untreated plates was significantly higher than that of the coated plates. Furthermore, the corrosion rates in both groups exhibited an initial gradual increase, followed by a decline to a stabilized level. In the blank group, the corrosion rate increased from an initial value of 0.368×10^{-3}/mpy to a peak of 9.72×10^{-3}/mpy on day 14. After stabilizing briefly, it decreased and finally plateaued at 3.43×10^{-3}/mpy. This trend may be attributed to the early-stage adhesion of SRB to the steel surface, where biofilm formation and continuous sulfide production accelerated corrosion. In later stages, the dense corrosion product layer formed on the steel surface isolated the plate from the environment, inhibiting further corrosion. In contrast, the corrosion rate of the Ag-ZnO nanoparticle-coated carbon steel increased slowly from an initial 0.52×10^{-3}/mpy, reaching a peak of 3.69×10^{-3}/mpy on day 18 (compared to that in the former group, the peak corrosion rate of the carbon steel in this group was reduced by approximately 62.04%). After stabilization, it declined and ultimately plateaued at 2.09×10^{-3}/mpy. This behavior may be ascribed to the effectiveness of the Ag-ZnO NP coating in mitigating SRB-induced corrosion. The dense biofilm-corrosion structure did not form rapidly on the coated steel surface, allowing partial exposure to the environment and continued reaction with hydrogen sulfide. Additionally, the Ag-ZnO NPs on the carbon steel surface exhibited antibacterial effects against SRB, reducing the viable SRB populations and thereby slowing corrosion.

Fig. 18 presents the SEM images of untreated carbon steel (Fig. 18(a)) and Ag-ZnO NP-coated samples (Fig. 18(b)) after SRB corrosion for 28 days, along with the EDS results of the corrosion products for untreated (Fig. 18(c)) and Ag-ZnO NP-coated (Fig. 18(d)) samples. The observations demonstrate severe uniform corrosion on the untreated carbon steel surface, whereas the Ag-ZnO NP-coated steel exhibited only localized pitting corrosion.

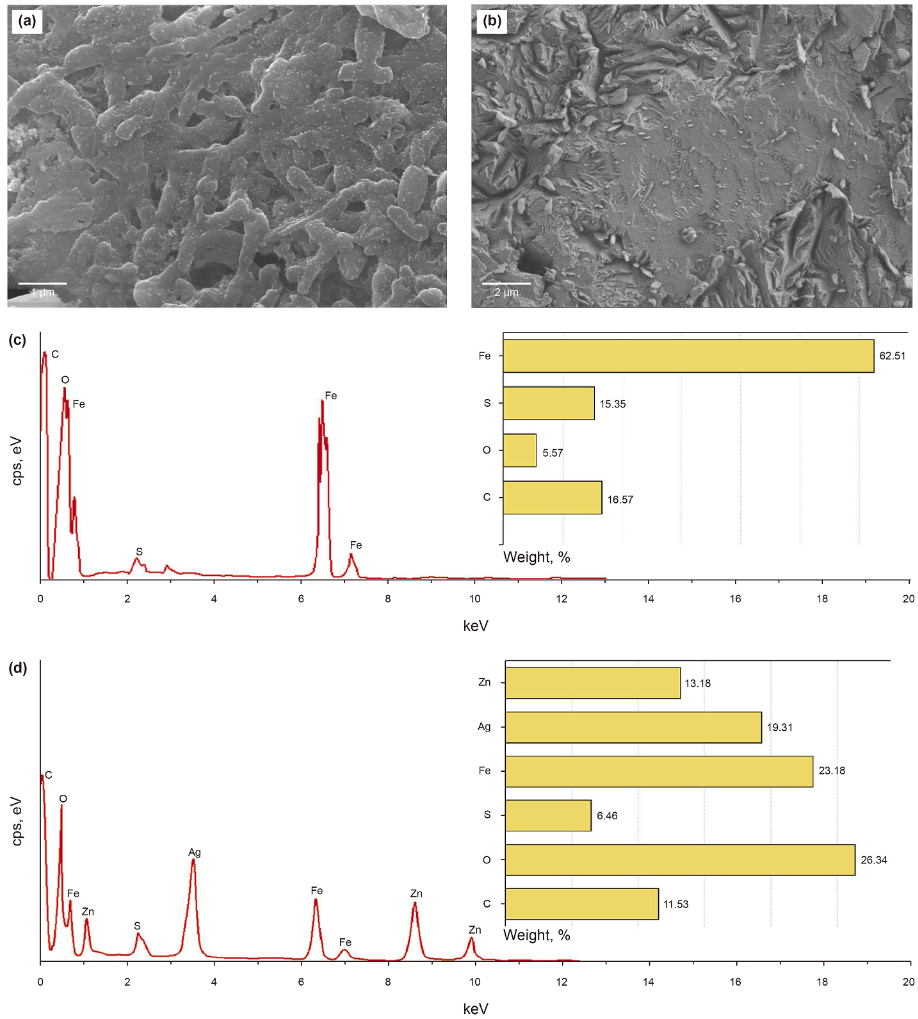

Fig. 18. SEM images of the carbon steel sheet before **(a)** and after **(b)** Ag-ZnO NP treatment, and **(c)**, **(d)** the EDS results of the SRB corrosion products peeled off from the steel surface.

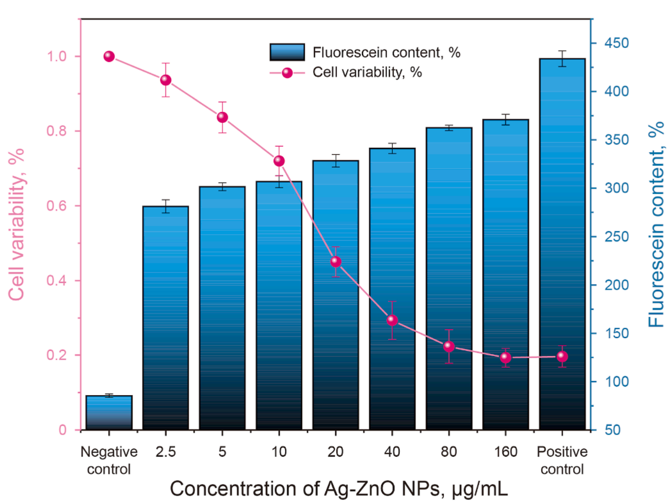

Fig. 19. Fluorescein content of SRB cells.

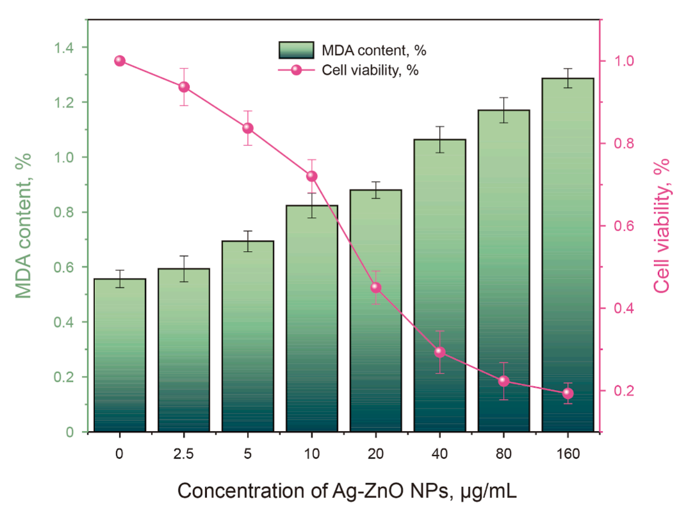

Fig. 20. MDA content of SRB cells.

This indicates that the Ag-ZnO NP coating provides excellent corrosion resistance, maintaining low and stable corrosion rates to prolong the lifespan of carbon steel. EDS results further revealed a significant reduction in FeS content within the corrosion products of the Ag-ZnO NP-coated group, attributable to the effective inhibition of SRB by the nanoparticles.

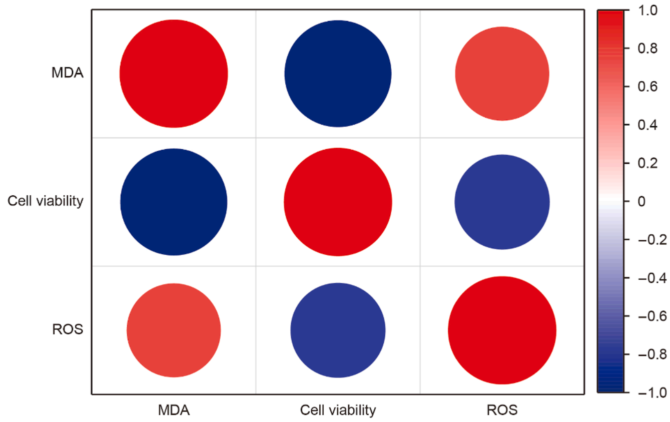

Fig. 21. Correlation analysis results of MDA, ROS, and activity, *$p < 0.05$.

4.12. Cell viability and oxidative damage assessment

Reactive oxygen species (ROS) is the general term for oxygen-containing free radicals and peroxides related to oxygen metabolism in organisms (Bedard and Krause, 2007). ROS production is inevitable for aerobic organisms, as it occurs at a controllable rate in healthy cells, and served as one of the criteria for determining whether cells are in a normal state to a certain extent (Zorov et al., 2014). To investigate whether ROS are associated with the antibacterial effects of Ag-ZnO NPs, we measured the ROS levels in untreated SRB cells and Ag-ZnO NP-treated SRB cells using the DCFH-DA fluorescent probe, with H_2O_2 included as a positive control to validate the accuracy of ROS measurements. Fig. 19 shows the cell viability values and DCF fluorescence probe detection results. As the nanoparticle concentration increased, the intracellular ROS content in SRB cells significantly exceeded that of the blank group, even reaching more than twice the original level. These results indicate that the Ag-ZnO NP treatment induced higher ROS production in the cells. Compared to that in the blank group, addition of Ag-ZnO NPs induced a sharp initial increase in the ROS levels in SRB cells. In contrast, as the concentration of Ag-ZnO NPs continued to increase, the cell viability of SRB gradually decreased to a very low range, clearly demonstrating that the nanoparticles caused a significant decline in cellular activity.

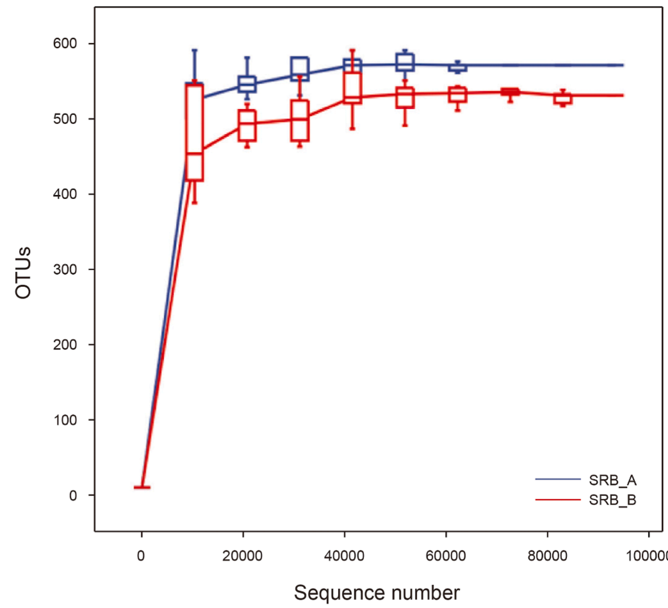

Fig. 23. Sparse graph of SRB_A and SRB_B.

To verify whether nanomaterials induce oxidative damage in bacterial cells through ROS, we investigated the lipid peroxidation levels of SRB membranes by measuring malondialdehyde (MDA) content. Fig. 20 illustrates the relationship between SRB cell viability values and MDA content under varying concentrations of Ag-ZnO NPs, clearly showing changes in MDA release and cell viability after 48 h of co-culturing SRB with different NP concentrations. The MDA content in the blank group of SRB cells remained low even after 48 h. With increasing concentrations of Ag-ZnO NPs, MDA levels showed a gradient rise, accompanied by a continuous decline in cell viability. Compared with that in Fig. 18, the increase in MDA observed here was more pronounced. This further suggests that SRB cells experienced acute peroxidation damage internally, rather than secondary ROS elevation caused by apoptosis, as ROS-generating organelles cease functioning during apoptotic processes. MDA content is a widely used indicator in studies on cellular senescence, stress resistance physiology, and oxidative stress severity, reflecting the extent of lipid peroxidation

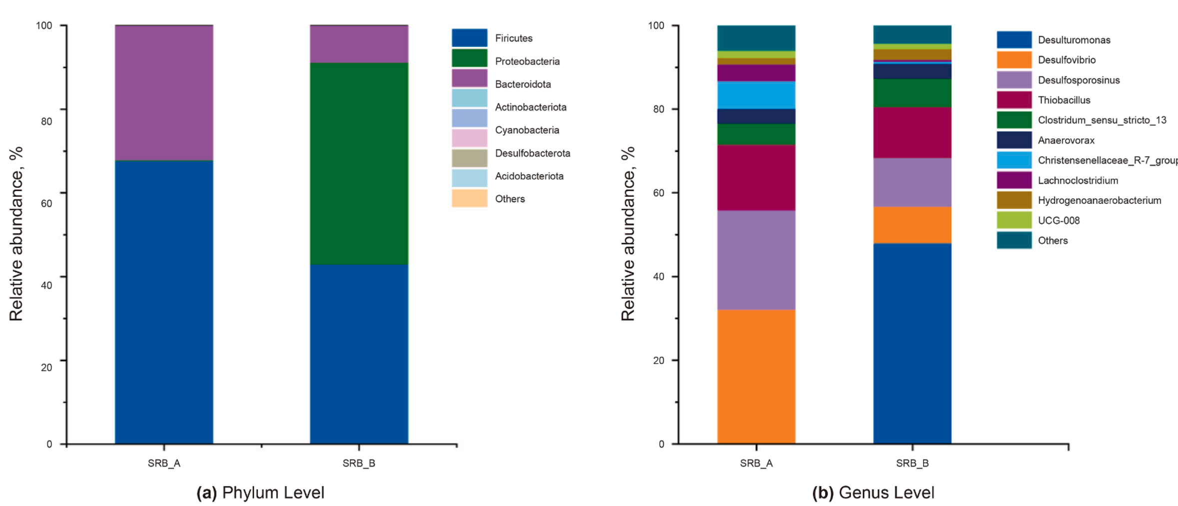

Fig. 22. Distribution of the SRB community structure at the **(a)** phylum level and **(b)** genus level.

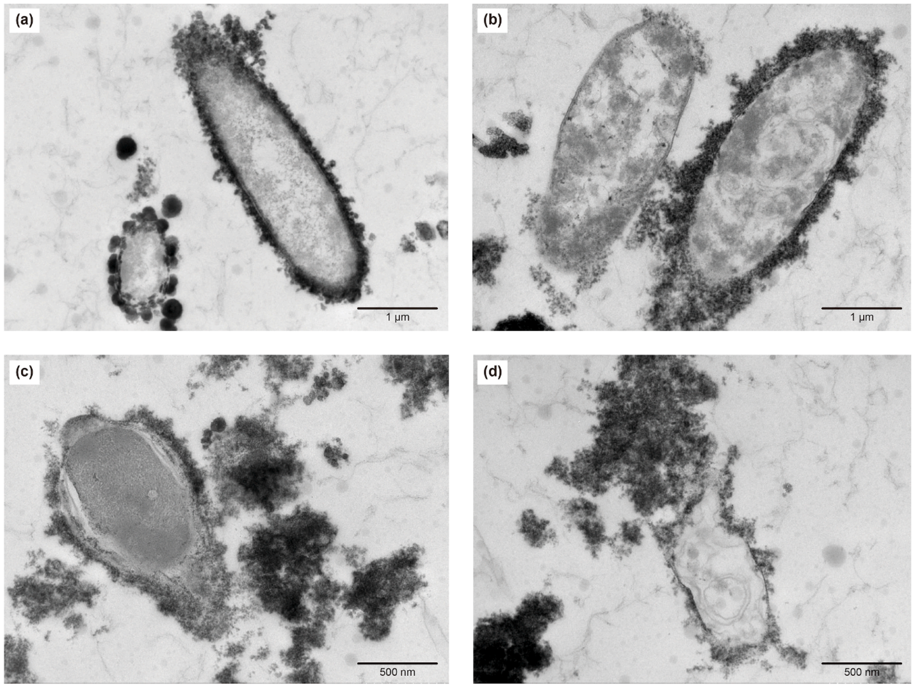

Fig. 24. Morphology of SRB with disrupted cell membrane.

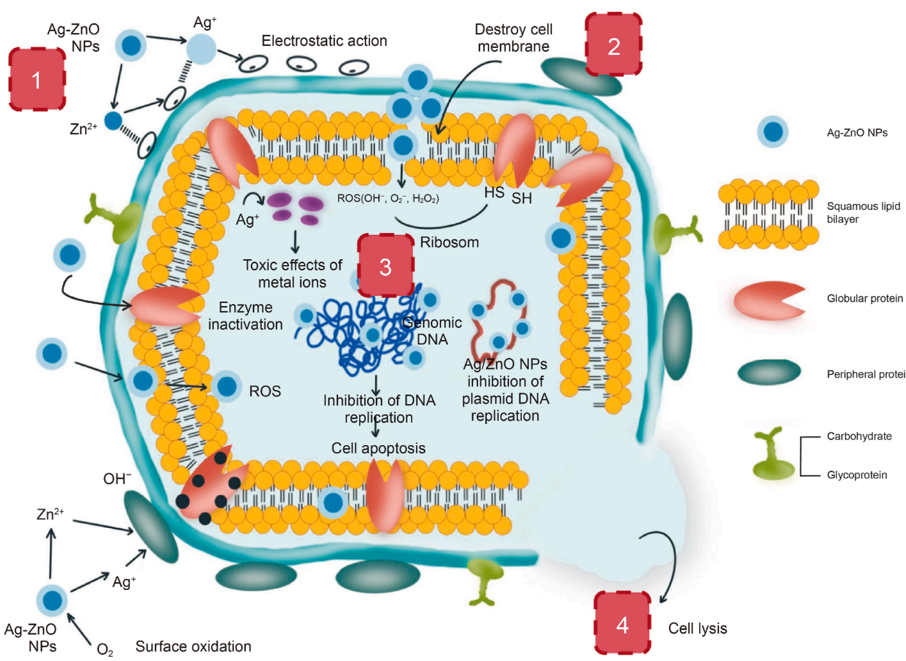

Fig. 25. Schematic diagram of the antibacterial mechanism of Ag-ZnO NPs.

in biomembranes (Wang et al., 2017). In organisms, free radicals trigger lipid peroxidation, producing MDA as an oxidative end product, which induces the cross-linking and polymerization of macromolecules like proteins and nucleic acids, leading to cytotoxicity (Blokhina et al., 2003). Additionally, MDA, as a lipid peroxidation end product, can impair mitochondrial respiratory chain complexes and key enzyme activities both in vivo and in vitro (Jakubczyk et al., 2020), whereas lipid peroxidation byproducts directly disrupt cell membranes and form protein adducts (Tirani and Haghjou, 2019), exacerbating cellular and tissue damage. In summary, MDA is a critical marker of membrane lipid peroxidation, and its accumulation aggravates membrane injury. Detection of MDA levels thus allows quantification of cellular damage. Overall, Ag-ZnO nanocomposites significantly induce oxidative damage in bacterial cells. A correlation analysis ($*p < 0.05$) of the three datasets mentioned above is presented in Fig. 21, which clearly demonstrates a strong positive correlation between intracellular ROS and MDA levels in SRB cells with increasing Ag-ZnO NP concentrations, whereas cell viability shows a negative correlation with both parameters.

4.13. Changes in the SRB community

This experiment involves two samples, of which SRB_A represents the control group without Ag-ZnO NP treatment and SRB_B represents the sample treated with Ag-ZnO NPs. Based on high-throughput sequencing technology to analyze the composition of bacterial communities in the samples, Fig. 22 shows the distribution of the dominant community structure in SRB_ A and SRB_B.

At the phylum level, compared to that in SRB_A, the proportion of *Firmicutes* and *Bacteroidota* decreased significantly, whereas the proportion of *Proteobacteria* increased relatively in SRB_B. This may be attributed to the presence of nanoparticles inhibiting some harmful bacteria and changing the microbial living environment, thereby promoting the growth of certain microorganisms. At the genus level, the difference in the community composition of SRB_A and SRB_B is rather significant. *Desulfuromonas*, *Desulfovibrio*, *Desulfosporosinus*, and *Thiobacillus* account for a relatively high proportion of dominant bacterial species; compared to that in SRB_A, the proportion of *Desulfovibrio*, *Desulfosporosinus*, and *Thiobacillus* decreased significantly in SRB_B, whereas the proportion of *Desulfuromonas* increased significantly, indicating that Ag-ZnO NPs have a better inhibitory effect on the former.

Alpha diversity refers to the indicators of species richness, diversity, and evenness in locally uniform habitats, also known as within-habitat diversity. Feature richness was estimated based on the Chao1 index and sparse curve plots of two samples were drawn (Fig. 23). Sparse curve plots can to some extent, reflect the level of sample diversity. Therefore, the diversity of samples treated with Ag-ZnO NPs can be intuitively concluded to be significantly lower than that of untreated samples, undoubtedly because of the strong interference of Ag-ZnO NPs. In summary, this further demonstrates the inhibitory effect of Ag-ZnO NPs on SRB.

4.14. Antibacterial mechanism of Ag-ZnO NPs

Fig. 24 shows the morphology of SRB cells treated with Ag-ZnO NPs. Ag-ZnO NPs adhere to the outer membrane of SRB cells and gradually enter the cell interior until severe membrane damage and cell lysis occur. A preliminary exploration was conducted on the antibacterial mechanism of Ag-ZnO NPs based on this experimental study (Fig. 25). Four possible ways have been identified in which Ag-ZnO NPs can promote bacterial cell death and inhibit cell activity.

i) Electrostatic effect: Ag-ZnO NPs have a higher specific surface area than that of ordinary materials, and silver ions (Ag^{+}) and zinc ions (Zn^{2+}) released during surface oxidation can directly interact with bacterial cell membranes or through electrostatic interactions between the released metal ions and negatively charged bacterial cell walls (Abebe et al., 2020).

ii) Destruction of bacterial cell membranes: The activity of proteins and enzymes decreases. Within cells, a significant increase in ROS content can alter the membrane protein or enzyme activity to disrupt bacterial cell membranes, inducing damage to the membrane protein and lipid bilayer (Jiang et al., 2009). As measured using the DCFH-DA fluorescence probe, the ROS content in SRB cells treated with nanomaterials increased greatly, even more than double that in the original. Upon comparing the data of MDA content in the blank group and SRB cells treated with nanomaterials, the MDA content in the treated SRB cells was found to have increased significantly. This substantial increase in ROS and MDA contents may be a primary reason for the cell membrane damage caused by Ag-ZnO NPs, consistent with previous research results reported by Raghupathi et al. (2011).

iii) Toxic effects of metal ions. A large number of metal ions pass through the cell membrane and enter the interior of bacterial cells. When the concentration of Ag^{+} and Zn^{2+} reaches a certain level, the positive charges carried by the two metal ions change the polarization state inside and outside the normal biofilm, causing a difference in the ion concentration inside and outside the bacterial cell membrane, hindering the transportation of nutrients required by cells, and leading to metabolic instability and cell damage (Pasquet et al., 2015). Further, Ag^{+} and Zn^{2+} are considered toxic. After entering the cell, they also cause protein denaturation and enzyme inactivation, inhibit DNA replication, cause cell dysfunction, and ultimately lead to bacterial apoptosis (Aranda et al., 2013).

iv) Cell lysis. The synergistic effect of the three abovementioned mechanisms continuously accelerates the process of bacterial cell membrane damage, to a certain extent, leading to complete cell membrane rupture, leakage of cell contents, and cell apoptosis.

5. Conclusion

Simple and green synthesis of Ag-ZnO NPs was achieved using *B. subtilis* without adding additional reducing agents, and applied to the suppression of oilfield SRB. Ag-ZnO NPs were nearly spherical in shape, with diameters between 33 and 35 nm. EDS, XRD, XPS, and FTIR analyses confirmed the biosynthesis of Ag-ZnO NPs and NP-stabilizing organic substances. The enzyme activity assay confirmed the presence of protease, amylase, and CL in *B. subtilis* suspension, among which protease is most likely involved in the nano-synthesis process. The excellent inhibitory effect of Ag-ZnO NPs on the diversity community of SRB was verified. The growth of SRB was effectively inhibited when the concentration of Ag-ZnO NPs reached 40 μg/mL. The corrosion rate of carbon steel sheets treated with Ag-ZnO nanoparticles was significantly lower than that of untreated carbon steel sheets. This indicates that Ag-ZnO NP can extend the time it takes for SRB to corrode carbon steel, thereby stabilizing the corrosion rate at a lower level and increasing the lifespan of the carbon steel.

1. A deficiency lies in the need for further exploring the relationship between the metal doping ratio and antibacterial effect considering the costs. Future studies are also needed to determine whether these NPs can induce pathogenic bacteria to mutate, whether they can pose potential harm to humans and a potential risk to nature.
2. The Ag component in Ag-ZnO NPs may react with H_2S under specific conditions to form Ag_2S precipitates. However, this behavior is closely related to multiple factors, including H_2S concentration, the diversity of SRB communities, and the environmental pH of the SRB habitat. The inhibitory effect of Ag-ZnO NPs on SRB cells and the stability of the NPs themselves should thus be considered together. To enhance stability, using composite NPs incorporating magnetic elements should be considered to significantly facilitate the recovery of Ag-ZnO NPs and address environmental safety concerns.
3. The toxic effects of Ag-ZnO NPs on both SRB and non-SRB should be considered. Investigating whether Ag-ZnO NPs preferentially disrupt SRB-specific metabolic pathways (e.g., the dissimilatory sulfite reductase DsrAB) while exerting minimal effects on core metabolic enzymes in non-SRB (such as those involved in the TCA cycle) is important for understanding

the ecological safety and stability of reservoir microbial communities.

CRediT authorship contribution statement

Yin-Fang Si: Writing – original draft, Data curation. **Yu-Long Liu:** Methodology, Data curation. **Fan Zhang:** Investigation, Conceptualization, Visualization. **Hao Dong:** Software, Visualization. **Qing Feng:** Methodology. **Xiao-Nan Li:** Validation. **Yue-Hui She:** Writing – review & editing, Funding acquisition. **Shan-Shan Sun:** Writing – review & editing.

Ethics approval and consent to participate

Not applicable.

Consent for publication

Not applicable.

Availability of data and materials

The data that support the findings of this study are available from the corresponding author, upon reasonable request.

Funding

This research was financially supported by the National Natural Science Foundation of China (No. 52474053, 52474028), and Open Fund of Hubei Key Laboratory of Oil and Gas Drilling and Production Engineering (Yangtze University) (No. YQZC202308).

Declaration of competing interest

The authors declare that they have no known competing financial interests or personal relationships that could have appeared to influence the work reported in this paper.

References

Abebe, B., Murthy, H.A., Amare, E., et al., 2020. Enhancing the photocatalytic efficiency of ZnO: Defects, heterojunction, and optimization. Environmental nanotechnology 14, 100336. https://doi.org/10.1016/j.enmm.2020.100336.
Agarwal, P., Gupta, R., Agarwal, N., et al., 2019. Advances in synthesis and applications of microalgal nanoparticles for wastewater treatment. J. Nanotechnol. 2019, 7392713. https://doi.org/10.1155/2019/7392713.
Alshamsi, H.A.H., Hussein, B.S., 2018. Hydrothermal preparation of silver doping zinc oxide nanoparticles: study the characterization and photocatalytic activity. Orient. J. Chem. 4 (34), 1898. https://doi.org/10.13005/ojc/3404025.
Aranda, A., Sequedo, L., Tolosa, L., et al., 2013. Dichloro-dihydro-fluorescein diacetate (DCFH-DA) assay: a quantitative method for oxidative stress assessment of nanoparticle-treated cells. Toxicol. Vitro 2 (27), 954–963. https://doi.org/10.1016/j.tiv.2013.01.016.
Ashar, A., Bhatti, I.A., Ashraf, M., et al., 2019. Fe^{3+}@ZnO/polyester based solar photocatalytic membrane reactor for abatement of RB5 dye. J. Clean. Prod. 246, 119010. https://doi.org/10.1016/j.jclepro.2019.119010.
Bedard, K., Krause, K.H., 2007. The NOX family of ROS-generating NADPH oxidases: physiology and pathophysiology. Physiol. Rev. 1 (87), 245–313. https://doi.org/10.1152/physrev.00044.2005.
Blokhina, O., Virolainen, E., Fagerstedt, K.V., et al., 2003. Antioxidants, oxidative damage and oxygen deprivation stress: A review. Ann. Bot. 2 (91), 179–194. https://doi.org/10.1093/aob/mcf118.
Breijyeh, Z., Jubeh, B., Karaman, R., et al., 2020. Resistance of gram-negative bacteria to current antibacterial agents and approaches to resolve it. Molecules 6 (25), 1340. https://doi.org/10.3390/molecules25061340.
Castaneda, H., Benetton, X.D., 2008. SRB-biofilm influence in active corrosion sites formed at the steel-electrolyte interface when exposed to artificial seawater conditions. Corros. Sci. 4 (50), 1169–1183. https://doi.org/10.1016/j.corsci.2007.11.032.
Chen, R., Li, Y., Sun, X., et al., 2015. Three metaltolerance Halobacillus sp. isolated from salt lakes in shaanxi,China. J. Microbiol. 35 (6), 38–43. https://doi.org/10.3969/j.issn.1005-7021.2015.06.007.
Chen, J., Zhu, Y., Fu, G., et al., 2016. High-level intra- and extra-cellular production of d-psicose 3-epimerase via a modified xylose-inducible expression system in Bacillus subtilis. J. Ind. Microbiol. Biotechnol. 11 (43), 1577–1591. https://doi.org/10.1007/s10295-016-1819-6.
Cliff, G., Lorimer, G.W., 1975. The quantitative analysis of thin specimens. J. Microsc. 2 (103), 203–207. https://doi.org/10.1111/j.1365-2818.1975.tb03895.x.
Datta, A., Patra, C., Bharadwaj, H., et al., 2017. Green synthesis of zinc oxide nanoparticles using parthenium hysterophorus leaf extract and evaluation of their antibacterial properties. J. Biotechnol. Biomater. 7 (3), 100271. https://doi.org/10.4172/2155-952X.1000271.
Dong, Z.H., Shi, W., Ruan, H.M., et al., 2011. Heterogeneous corrosion of mild steel under SRB-biofilm characterised by electrochemical mapping technique. Corros. Sci. 9 (53), 2978–2987. https://doi.org/10.1016/j.corsci.2011.05.041.
Dugassa, J., Shukuri, N., 2017. Review on antibiotic resistance and its mechanism of development. Journal of Health, Medicine Nursing 3 (1), 1–17.
Edwards, D., Rowlands, N., Guarrera, D., et al., 2014. Investigation of multiple, large area EDS detectors on an SEM capable of various mounting geometries for optimal EDS analysis. Microsc. Microanal. S3 (20), 646–647. https://doi.org/10.1017/S1431927614004954.
Enning, D., Venzlaff, H., Garrelfs, J., et al., 2012. Marine sulfate-reducing bacteria cause serious corrosion of iron under electroconductive biogenic mineral crust. Environ. Microbiol. 7, 14.
Estensmo, E.L.F., Maurice, S., Morgado, L., et al., 2021. The influence of intraspecific sequence variation during DNA metabarcoding: A case study of eleven fungal species. Molecular Ecology Resources 4 (21), 1141–1148. https://doi.org/10.1111/1755-0998.13329.
Feng, Y.Y., Zhao, Z.C., Yang, W.B., et al., 2021. Microbial natural synthetic metal nanoparticles and the application in heavy oil catalytic viscosity reduction. Chem. Ind. Eng. Prog. 4 (40), 2215–2226. https://doi.org/10.16085/j.issn.1000-6613.2020-1611 (in Chinese).
Ghosh, S., Goudar, V., Padmalekha, K., et al., 2012. ZnO/Ag nanohybrid: synthesis., characterization., synergistic antibacterial activity and its mechanism. RSC Adv. 3 (2), 930–940. https://doi.org/10.1039/C1RA00815C.
Gopinath, V., Velusamy, P., 2013. Extracellular biosynthesis of silver nanoparticles using Bacillus sp. GP-23 and evaluation of their antifungal activity towards Fusarium oxysporum. Spectrochim. Acta Mol. Biomol. Spectrosc. 106, 170–174. https://doi.org/10.1016/j.saa.2012.12.087.
Gu, T., Jia, R., Unsal, T., et al., 2019. Toward a better understanding of microbiologically influenced corrosion caused by sulfate reducing bacteria. J. Mater. Sci. Technol. 4 (35), 169–174 (in Chinese). Doi: CNKI:SUN:CLKJ.0.2019-04-022.
Haas, B.J., Gevers, D., Earl, A.M., et al., 2011. Chimeric 16S rRNA sequence formation and detection in Sanger and 454-pyrosequenced PCR amplicons. Genome Res. 3 (21), 494–504. https://doi.org/10.1101/gr.112730.110.
Harinee, S., Muthukumar, K., James, R., et al., 2022. Bio-approach ZnO/Ag nanoflowers: enhanced photocatalytic and photoexcited anti-microbial activities towards pathogenic bacteria. Mater. Today Sustain. (18), 100–133. https://doi.org/10.1016/j.mtsust.2022.100133.
Indhira, D., Krishnamoorthy, M., Ameen, F., et al., 2022. Biomimetic facile synthesis of zinc oxide and copper oxide nanoparticles from Elaeagnus indica for enhanced photocatalytic activity. Environ. Res. 212, 113323. https://doi.org/10.1016/j.envres.2022.113323.
Iqbal, H., Fatima, A., Khan, H.A.A., et al., 2022. ZnO nanoparticles produced in the culture supernatant of Bacillus thuringiensis ser. israelensis affect the demographic parameters of Musca domestica using the age-stage, two-sex life table. Pest Manag. Sci. 4, 78. https://doi.org/10.1002/ps.6783.
Jakubczyk, K., Dec, K., Kałduńska, J., et al., 2020. Reactive oxygen species-sources, functions, oxidative damage. Polski Merkuriusz Lekarski. Organ Polskiego Towarzystwa Lekarskiego 284 (48), 124–127.
Jiang, W., Mashayekhi, H., Xing, B., et al., 2009. Bacterial toxicity comparison between nano-and micro-scaled oxide particles. Environ. Pollut. 5 (157), 1619–1625. https://doi.org/10.1016/j.envpol.2008.12.025.
Jiang, Y., Gao, X., Yang, X., et al., 2024. Sulfate-reducing bacteria (SRB) mediated carbonate dissolution and arsenic release: Behavior and mechanisms. Sci. Total Environ. 929, 172572. https://doi.org/10.1016/j.scitotenv.2024.172572.
Khan, M., Hussain, M., Djavanroodi, F., 2021. Microbiologically influenced corrosion in oil and gas industries: a review. Int. J. Corros. Scale Inhib. 1 (10), 80–106. https://doi.org/10.17675/2305-6894-2021-10-1-5.
Mahdi, Z.S., Talebnia Roshan, F., Nikzad, M.E.H., et al., 2021. Biosynthesis of zinc oxide nanoparticles using bacteria: a study on the characterization and application for electrochemical determination of bisphenol A. Inorganic Nano-Metal Chemistry 9 (51), 1249–1257. https://doi.org/10.1080/24701556.2020.1835962.
Marciales, A., Peralta, Y., Haile, T., et al., 2019. Mechanistic microbiologically influenced corrosion modeling—A review. Corros. Sci. 146, 99–111. https://doi.org/10.1016/j.corsci.2018.10.004.
Nasiri, V., Dalimi, A., Ghaffarifar, F., et al., 2017. LB broth-lyophilized Rabbit serum (LLR) as a new and suitable culture medium for cultivation of promastigotes of Leishmania major. J. Parasit. Dis. 1 (41), 247–251. https://doi.org/10.1007/s12639-016-0786-1.
Newbury, D.E., Ritchie, N.W., 2013. Is scanning electron microscopy/energy dispersive X-ray spectrometry (SEM/EDS) quantitative? Scanning 3 (35), 141–168. https://doi.org/10.1002/sca.21041.
Nwodo, U.U., Green, E., Okoh, A.I., et al., 2017. Bacterial exopolysaccharides: functionality and prospects. Int. J. Mol. Sci. 13 (11), 14002–14015. https://doi.org/10.3390/ijms131114002.

Okamoto, H., Kawamura, G., Kudo, T., et al., 1983. Study of oxygen adsorption on platinum through observation of exchange current in a solid electrolyte concentration cell. Electrochim. Acta 3 (28), 379–382. https://doi.org/10.1002/chin.198324022.
Ovais, M., Khalil, A.T., Ayaz, M., et al., 2018. Biosynthesis of metal nanoparticles via microbial enzymes: a mechanistic approach. Int. J. Mol. Sci. 12 (19), 4100. https://doi.org/10.3390/ijms19124100.
Park, H.H., Zhang, X., Lee, K.W., et al., 2015. Selective photochemical synthesis of Ag nanoparticles on position-controlled ZnO nanorods for the enhancement of yellow-green light emission. Nanoscale 48 (7), 20717–20724. https://doi.org/10.1039/C5NR05877E.
Parvekar, P., Palaskar, J.N., Metgud, S., et al., 2020. The minimum inhibitory concentration (MIC) and minimum bactericidal concentration (MBC) of silver nanoparticles against Staphylococcus aureus. Biomaterial Investigations in Dentistry 1 (7), 105–109. https://doi.org/10.1080/26415275.2020.1796674.
Pascariu, P., Cojocaru, C., Samoila, P., et al., 2020. Photocatalytic and antimicrobial activity of electrospun ZnO: Ag nanostructures. J. Alloys Compd. 834, 155144. https://doi.org/10.1016/j.jallcom.2020.155144.
Pasquet, J., Chevalier, Y., Couval, E., et al., 2015. Zinc oxide as a new antimicrobial preservative of topical products: Interactions with common formulation ingredients. Int. J. Pharm. 479 (1), 88–95. https://doi.org/10.1016/j.ijpharm.2014.12.031.
Porter, T.M., Hajibabaei, M., 2018. Scaling up: A guide to high-throughput genomic approaches for biodiversity analysis. Mol. Ecol. 27 (1), 313–338. https://doi.org/10.1111/mec.14478.
Potlog, T., Duca, D., Dobromir, M., 2015. Temperature-dependent growth and XPS of Ag-doped ZnTe thin films deposited by close space sublimation method. Appl. Surf. Sci. (352), 33–37. https://doi.org/10.1016/j.apsusc.2015.03.133.
Puhazhselvan, P., Aparna, R., Ayyadurai, N., et al., 2017. Enzyme based cleaner process for enhanced recovery of lipids from tannery fleshing waste. J. Clean. Prod. 144, 187–191. https://doi.org/10.1016/j.jclepro.2016.12.148.
Raghupathi, K.R., Koodali, R.T., Manna, A.C., et al., 2011. Size-dependent bacterial growth inhibition and mechanism of antibacterial activity of zinc oxide nanoparticles. Langmuir 7 (27), 4020–4028. https://doi.org/10.1021/la104825u.
Rasheed, P.A., Jabbar, K.A., Mackey, H.R., et al., 2019. Recent advancements of nanomaterials as coatings and biocides for the inhibition of sulfate reducing bacteria induced corrosion. Curr. Opin. Chem. Eng. (25), 35–42. https://doi.org/10.1016/j.coche.2019.06.003.
Rasool, K., Nasrallah, G., Younes, N., et al., 2018. "Green" ZnO-interlinked chitosan nanoparticles for the efficient inhibition of sulfate-reducing bacteria in inject seawater. ACS Sustain. Chem. Eng. 6 (3), 7b04248. https://doi.org/10.1021/acssuschemeng.7b04248.
Reddy, K.V., Sree, N.R.S., Kumar, P.S., et al., 2022. Microbial Enzymes in the Biosynthesis of Metal Nanoparticles. Ecological Interplays in Microbial Enzymology. Springer, pp. 329–350.
Rtimi, S., Dionysiou, D.D., Pillai, S.C., et al., 2019. Advances in catalytic/photocatalytic bacterial inactivation by nano Ag and Cu coated surfaces and medical devices. Appl. Catal. B Environ. 240, 291–318. https://doi.org/10.1016/j.apcatb.2018.07.025.
Satyavani, K., Gurudeeban, S., Ramanathan, T., et al., 2011. Biomedical potential of silver nanoparticles synthesized from calli cells of Citrullus colocynthis (L.) Schrad. J. Nanobiotechnol. 9, 43. https://doi.org/10.1186/1477-3155-9-43.
Sayadi, M.H., Sobhani, S., Shekari, H., et al., 2019. Photocatalytic degradation of azithromycin using $GO@Fe_3O_4/ZnO/SnO_2$ nanocomposites. J. Clean. Prod. 232, 127–136. https://doi.org/10.1016/j.jclepro.2019.05.338.
Scimeca, M., Bischetti, S., Lamsira, H.K., et al., 2018. Energy dispersive X-ray (EDX) microanalysis: a powerful tool in biomedical research and diagnosis. Eur. J. Histochem. 62 (1), 2841. https://doi.org/10.15436/2475-6245.16.ED945, 2841.
Sezonov, G., Joseleau-Petit, D., D'Ari, R., et al., 2007. Escherichia coli physiology in luria-bertani broth. J. Bacteriol. 189 (23), 8746–8749. https://doi.org/10.1128/JB.01368-07.
Shao, D., Wei, Q., 2018. Microwave-assisted rapid preparation of nano-ZnO/Ag composite functionalized polyester nonwoven membrane for improving its UV shielding and antibacterial properties. Materials 8 (11), 1412. https://doi.org/10.3390/ma11081412.
Sherar, B.W., Power, I.M., Keech, P.G., et al., 2011. Characterizing the effect of carbon steel exposure in sulfide containing solutions to microbially induced corrosion. Corros. Sci. 53 (3), 955–960. https://doi.org/10.1016/j.corsci.2010.11.027.
Si, Y., Wang, B., Zhang, F., et al., 2024. Bacillus subtilis-mediated synthesis of ZnO and Ag-ZnO nanoparticles for eco-friendly displacement agents: enhancing oil recovery in middle/low permeability reservoirs with nanofluid. Phys. Fluids 36 (11), 19. https://doi.org/10.1063/5.0226969.
Siddiqi, K.S., Husen, A., Rao, R.A., et al., 2018. A review on biosynthesis of silver nanoparticles and their biocidal properties. J. Nanobiotechnol. 16 (1), 14. https://doi.org/10.1186/S12951-018-0334-5.
Sirelkhatim, A., Mahmud, S., Seeni, A., et al., 2015. Review on zinc oxide nanoparticles: antibacterial activity and toxicity mechanism. Nano-Micro Lett. (7), 219–242. https://doi.org/10.1007/s40820-015-0040-x.
Stankic, S., Suman, S., Haque, F., et al., 2016. Pure and multi metal oxide nanoparticles: synthesis, antibacterial and cytotoxic properties. J. Nanobiotechnol. 14, 1–20 doi: 1186/s12951-016-0225-6.
Su, Y., Liu, C., Fang, H., et al., 2020. Bacillus subtilis: a universal cell factory for industry, agriculture, biomaterials and medicine. Microb. Cell Fact. (19), 1–12. https://doi.org/10.1186/s12934-020-01436-8.
Subhan, M.A., Awal, M., Ahmed, T., et al., 2014. Photocatalytic and antibacterial activities of Ag/ZnO nanocomposities fabricated by co-precipitation method. Acta Metall. Sin. (27), 223–232. https://doi.org/10.1007/s40195-014-0038-2.
Sun, H., Yang, Z., Pu, Y., et al., 2019. Zinc oxide/vanadium pentoxide heterostructures with enhanced day-night antibacterial activities. J. Colloid Interface Sci. 547, 10. https://doi.org/10.1016/j.jcis.2019.03.061.
Thabit, H.A., Kabir, N.A., Ismail, A.K., et al., 2022. Development of Ag-doped ZnO thin films and thermoluminescence (TLD) characteristics for radiation technology. Nanomaterials 17 (12), 3068. https://doi.org/10.3390/nano12173068.
Tirani, M., Haghjou, M., 2019. Reactive oxygen species (ROS), total antioxidant capacity (AOC) and malondialdehyde (MDA) make a triangle in evaluation of zinc stress extension. J. Animal Plant Sci. 29 (3), 1100–1111.
Tripathy, A., Raichur, A.M., Chandrasekaran, N., et al., 2010. Process variables in biomimetic synthesis of silver nanoparticles by aqueous extract of Azadirachta indica (Neem) leaves. J. Nanoparticle Res. 12, 237–246. https://doi.org/10.1007/s11051-009-9602-5.
Utgikar, V.P., Chen, B.Y., Chaudhary, N., et al., 2001. Acute toxicity of heavy metals to acetate-utilizing mixed cultures of sulfate-reducing bacteria: EC100 and EC50. Environ. Toxicol. Chem. 12 (20), 2662–2669. https://doi.org/10.1897/1551-5028(2001)020<2662:ATOHMT>2.0.CO;2.
Utgikar, V.P., Harmon, S.M., Chaudhary, N., et al., 2002. Inhibition of sulfate-reducing bacteria by metal sulfide formation in bioremediation of acid mine drainage. Environ. Toxicol. 17 (1), 40–48. https://doi.org/10.1002/tox.10031.
Wang, S., Wu, J., Yang, H., et al., 2017. Antibacterial activity and mechanism of Ag/ZnO nanocomposite against anaerobic oral pathogen Streptococcus mutans. J. Mater. Sci. Mater. Med. (28), 1–8. https://doi.org/10.1007/s10856-016-5837-8.
Xu, D., Li, Y.C., Gu, T.Y., et al., 2016. Mechanistic modeling of biocorrosion caused by biofilms of sulfate reducing bacteria and acid producing bacteria. Bioelectrochemistry 110, 52–58. https://doi.org/10.1016/j.bioelechem.2016.03.003.
Yousefi, R., Jamali-Sheini, F., Cheraghizade, M., et al., 2015. Enhanced visible-light photocatalytic activity of strontium-doped zinc oxide nanoparticles. Mater. Sci. Semicond. Process. 32, 152–159. https://doi.org/10.1016/j.mssp.2015.01.013.
Yusof, H.M., Mohamad, R., Zaidan, U.H., et al., 2020. Sustainable microbial cell nanofactory for zinc oxide nanoparticles production by zinc-tolerant probiotic Lactobacillus plantarum strain TA4. Microb. Cell Fact. 19, 10. https://doi.org/10.1186/s12934-020-1279-6.
Zheng, Y., Zheng, L., Zhan, Y., et al., 2007. Ag/ZnO heterostructure nanocrystals: synthesis, characterization, and photocatalysis. Inorg. Chem. 46 (17), 6980–6986. https://doi.org/10.1021/ic700688f.
Zorov, D.B., Juhaszova, M., Sollott, S.J., et al., 2014. Mitochondrial reactive oxygen species (ROS) and ROS-induced ROS release. Physiol. Rev. 3 (94), 909–950. https://doi.org/10.1152/physrev.00026.2013.